Cellular/Molecular

Morphology and Dendrite-Specific Synaptic Properties of Midbrain Neurons Shape Multimodal Integration

S. Weigel,[1]* **T. Kuenzel,**[2]* **K. Lischka,**[1,3] **G. Huang,**[1,4] **and H. Luksch**[1]

[1]Chair of Zoology, School of Life Sciences Weihenstephan, Research Department Molecular Life Sciences, Technical University Munich, Freising 85354, Germany, [2]Auditory Neurophysiology Group, Department of Chemosensation, Rheinisch-Westfaelische Technische Hochschule Aachen University, Aachen 52074, Germany, [3]Department of Developmental Biology, Institute of Biology I, Faculty of Biology, University of Freiburg, Freiburg 79104, Germany, and [4]Department of Biophysics, Center for Integrative Physiology and Molecular Medicine, School of Medicine, Saarland University, Homburg 66421, Germany

Multimodal integration facilitates object recognition and response to sensory cues. This depends on spatiotemporal coincidence of sensory information, recruitment of NMDA-type glutamate receptors and inhibitory feedback. Shepherd's crook neurons (SCNs) in the avian optic tectum (TeO) are an ideal model for studying cellular mechanism of multimodal integration. They receive different sensory modalities through spatially segregated dendrites, are important for stimulus selection and have an axon-carrying dendrite (AcD). We performed whole-cell patch-clamp experiments in chicken midbrain slices of both sexes. We emulated visual and auditory input *in vitro* by stimulating presynaptic afferents electrically. Simultaneous stimulation enhanced responses inversely depending on stimulation amplitude demonstrating the principle of inverse effectiveness. Contribution of NMDA-type glutamate receptors prolonged postsynaptic events for visual inputs only, causing a strong modality-specific difference in synaptic efficacy. We designed a multicompartment model to study the effect of morphological and physiological parameters on multimodal integration by varying the distance between soma and axonal origin and the amount of NMDA receptor (NMDAR) contribution. These parameters changed the preference of the model for one input channel and adjusted the range of input rates at which multimodal enhancement occurred on naturalistic stimulation. Thus, the unique morphology and synaptic features of SCNs shape the integration of input at different dendrites and generates an enhanced multimodal response.

Key words: dendrite; midbrain; morphology; multimodal; NMDA; tectum

---

Significance Statement

Multimodal integration improves perception and responses to objects. The underlying cellular mechanism depends on a balance between excitation and inhibition, and NMDA-type glutamate receptors that are involved in the multiplicative nature of enhancement following the principle of inverse effectiveness. Based on a detailed analysis of an identified multimodal cell type in the vertebrate midbrain, we studied the influence of cellular morphology and unimodal synaptic properties on multimodal integration. We can show that the combination of cellular morphology and modality-specific synaptic properties including NMDA receptor (NMDAR) contribution is optimal for nonlinear, multimodal enhancement and determines the dynamic response range of the integrating neuron. Our findings mechanistically explain how synaptic properties and cellular morphology of a midbrain neuron contribute to multimodal enhancement.

Introduction

The integration of multisensory information from the same object into a congruent representation in the brain has been intensely studied in the past decades from the level of single neurons to behavior (Angelaki et al., 2009; Stein et al., 2020). Multimodality enhances the sensory representation of congruent stimuli, facilitates the localization of potential danger or conspecifics, and shortens response latencies (Rowland et al., 2007b; Gingras et al., 2009; Stein et al., 2014; Felch et al., 2016; Verhaal and Luksch, 2016b; Truszkowski et al., 2017). Multisensory integration can lead to responses that are comparable, weaker or

greater than the sum of the individual responses (Meredith and Stein, 1986; Stein and Stanford, 2008; Stein et al., 2009, 2014). Excitatory inputs activating NMDA-type glutamate receptors and local or global inhibitory feedback can both contribute to the nonlinear nature of multimodal enhancement (Meredith et al., 1987; Binns and Salt, 1996; Stein and Stanford, 2008; Zahar et al., 2009; Cuppini et al., 2010; Harwell et al., 2015; Felch et al., 2016; Kardamakis et al., 2016; Truszkowski et al., 2017).

The optic tectum (TeO) of birds is an attractive model to study cellular mechanisms of sensory integration. It is part of the midbrain and involved in many functions such as integrating different sensory modalities, movement initiation and sensory target selection (Knudsen et al., 1995; Karten et al., 1997; Luksch, 2003; Knudsen, 2007; Wylie et al., 2009; Sridharan and Knudsen, 2015). It is composed of 15 layers, each characterized by its cell-type specificity and connectivity (Luksch, 2003). Visual information is passed from the retina to the contralateral tectum via the optic tract and terminates in the retinorecipient layers 2–5 and 7 (Yamagata et al., 2006). Auditory stimuli are relayed to the deeper layers 10–13 from either the external part of the inferior colliculus (Knudsen and Knudsen, 1983; Pena and Gutfreund, 2014) or from an external portion of the formatio reticularis lateralis (FRLx; Niederleitner and Luksch, 2012; Niederleitner et al., 2017). Some tectal neurons responded to both visual and auditory input in barn owls and pigeons and showed multimodal enhancement (Knudsen, 1982; Lewald and Dörrscheidt, 1998; Zahar et al., 2009).

Few studies elucidate mechanisms of multimodal integration on the cellular level (Felch et al., 2016; Kardamakis et al., 2016; Truszkowski et al., 2017). The Shepherd's crook neuron (SCN) with its unique morphology offers an ideal basis to study these principles in single multimodal neurons. It has separated dendritic fields in both retinorecipient and deep tectal layers, an axon originating at the apical dendrite (Ramón y Cajal, 1909; Woodson et al., 1991; Triarhou, 2014; Garrido-Charad et al., 2018; Lischka et al., 2018), and was shown to transmit visual and auditory information to the nuclei isthmi (Maczko et al., 2006).

We investigated the responses of SCN to stimuli at the two different dendritic fields with whole-cell patch-clamp experiments combined with pharmacology and imaging methods. In these *in vitro* experiments, SCN showed bimodal enhancement. The amount of enhancement was inversely depending on the stimulus amplitude demonstrating the effect of inverse effectiveness. NMDA-type glutamate receptors differentially contributed to evoked EPSC in a dendrite-specific manner. We created a multi-compartment model constrained by the physiological data and morphologic characteristics of SCN to investigate the impact of the specific cellular features on multimodal integration. We found that the combination of morphology and modality-specific NMDA receptor (NMDAR) contribution favors nonlinear, super-additive enhancement with inverse effectiveness and that the interplay of these features adapted the dynamic response range of SCN to input characteristics.

Materials and Methods

Chicken hatchlings (1–6 d of age, White Leghorn) of both sexes were used. Animals were anesthetized with a mixture of ketamine (Ketamidor; Inresa Arzneimittel), and xylazinhydrochloride (Proxylaz; Bayer) at 37.5 and 5 mg/kg body weight before decapitation. All procedures conformed to National Institutes of Health guidelines on the ethical use of the animals, and were approved by the respective local authorities in Munich. All efforts were made to minimize both the suffering and the number of animals used in these experiments.

Slice preparation

Ice-cooled oxygenated artifical cerebrospinal fluid (aCSF) was used during brain preparation and brain slicing (120 mM NaCl, 3 mM KCl, 1 mM $MgCl_2$, 23 mM $NaHCO_3$, 1.2 mM NaH_2PO_4, 2 mM $CaCl_2$, 11 mM D-glucose; pH 7.4; osmolarity 305 mOsm; oxygenated with carbogen: 95% O_2 and 5% CO_2). After decapitation, the brain was removed from the skull, the midbrain was isolated and separated in two hemispheres. Each hemisphere was embedded in low-melting point agarose (Sigma, catalog #A4675-500G, 1.65% dissolved in HEPES puffer; 290 mM saccharose, 5 mM HEPES, 3 mM KCl, and 3 mM $MgCl_2·6H_2O$; pH 7.4), sectioned horizontally into 500-μm brain slices, and collected in oxygenated aCSF at room temperature (RT).

Whole-cell electrophysiology

Slices were immobilized on poly-D-lysine-coated coverslips and transferred to a slice chamber on a fixed stage microscope (E600FN, Nikon, or Axio Examiner, Zeiss) equipped with DIC infrared contrast mounted on a vibration-isolation table and perfused with oxygenated aCSF at RT.

Recording electrodes were produced from glass micropipettes (GB150F-8B, Science Products GmbH) on a horizontal puller (Model P-97, Sutter Instrument Company). They had resistances ranging from 3 to 8 MΩ when filled with internal solution (100 mM K-Gluconat, 40 mM KCl, 10 mM HEPES, 2 mM $MgCl_2·6H_2O$, 2 mM Mg-ATP, 1.1 mM EGTA, and 0.1 mM $CaCl_2·2H_2O$; pH 7.4) containing 0.5% biocytin-HCl, or DIOC16 (1 μM), or Lucifer yellow (1 mM). Osmolarity was adjusted to about 300 mOsm/l with glucose.

In parts of the experiments, the sodium channel blocker QX314 (1 mM, 552233, EMD Millipore) was added to the internal solution. To study the contribution of glutamate receptors, we added either D-APV (25 μM, BN0085, Biotrend) or NBQX (5 μM, N183, Sigma-Aldrich) to the ACSF solution.

Recordings were performed with an EPC-9 or EPC-10 patch clamp amplifier (HEKA, with either PULSE or PATCHMASTER software), and stored for offline analysis in MATLAB.

For all recordings, we clamped the neurons to a membrane potential of –70 mV. We excluded recordings in case of a series resistance >50 MΩ, a leak conductance >1 nS and an initial membrane potential >−40 mV.

Bipolar stimulation electrodes were manufactured from two twisted coated nichrome wires (uncoated diameter 51 μm, coated diameter 66 μm, Science Products GmbH), stabilized by acrylic glue, mounted inside a glass microcapillary, and connected to an isolated pulse stimulator (Model 2100, AM System). One stimulation electrode was positioned onto the upper layers (L1 to L4). Neurons were recorded in radial position to this electrode. To prevent antidromic stimulation of SCNs axons, we position the second stimulation electrode in layer 13 slightly laterally from the targeted neurons (Fig. 1). Extracellular stimuli usually consisted of bipolar pulses with 500 μs duration and 10 to 300 μA amplitude. We discarded neurons from analysis if postsynaptic potentials or action potentials (APs) overlap with stimulus artefacts (~1–2 ms after stimulus onset) indicating direct stimulation.

Whole-cell patch clamp data were imported to MATLAB R2016b or later versions (MathWorks) using ImportHEKALegacy script (J. Broeke, Vrije Universiteit Amsterdam) and further analyzed using custom-made scripts. All data were digitally filtered at 50 Hz. Membrane resistance was calculated from steady-state membrane voltages to hyperpolarizing current steps (−50 to 0 pA) and membrane time constant tau by single exponential fitting (exp2fit) the signal when membrane voltages recovered of these hyperpolarized states. Threshold currents are defined as the depolarizing current necessary to evoke the first AP.

Postsynaptic events evoked by extracellular stimulation measured in current clamp mode were analyzed as follows: we calculated a threshold (mean membrane potential in a 100 ms time window before stimulation plus 5 mV) to define latency (first time exceeding the threshold). For detecting the end of the signal, we smoothed the data with a window of 2.5 ms and determined the last sample above the threshold. APs were identified and characterized using the findpeaks function in MATLAB (MinPeakHeight: –20 mV, MinPeakDistance: 1 ms, MinPeakProminence: 10 mV). The reliability represents the percentage of repetitions with successfully evoked AP. We isolated
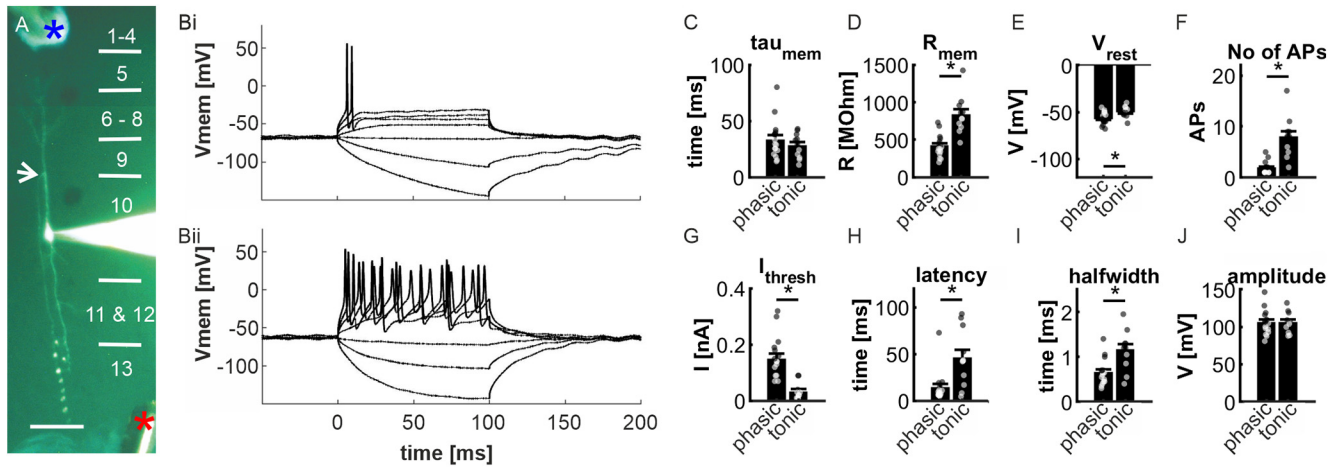
Figure 1. **A**, Intracellular labeled SCN (filled with Lucifer yellow) and positioning of stimulus electrodes. The axon origin on the apical dendrite is marked by an arrow. Borders of the tectal layers are indicated on the right. One stimulus electrode was positioned in layers 1–4 (blue asterisk) and a second stimulus electrode in layer 13 (red asterisk). Scale bar: 100 μm. **B**, Two exemplary whole-cell patch-clamp responses of SCN to different holding currents: (**Bi**) phasic response and (**Bii**) tonic response. Currents were applied as a step protocol starting at $t = 0$ ms ranging from −100 to 200 pA with 50 pA increase. **C–J**, Quantification of physiological parameters for phasic and tonic firing SCNs determined in current-clamp experiments. Bar plots of membrane time constant tau$_{mem}$ (**C**), input resistance R$_{mem}$ (**D**), resting membrane potential V$_{rest}$ (**E**), maximal number of evoked APs (**F**), minimal applied current necessary to evoke APs I$_{thresh}$ (**G**), latency of the first evoked AP at I$_{thresh}$ (**H**), half-maximal width of these APs (**I**), and their amplitude (**J**). Data are plotted as mean ± SEM; $n = 16$ (phasic) and $n = 11$ (tonic), asterisk indicate $p < 0.05$ (two-sided Wilcoxon rank-sum test). Individual data of each neuron is plotted as dots on the corresponding bars.

the APs in an 8.5-ms window (3.5 ms before AP peak and 5 ms after AP peak) and smoothed them with a Savitzky–Golay filter with a 0.25-ms frame length. We identified the starting point as the first point when the second derivative of the membrane potential was crossing a threshold (1× SD). The membrane potential at this point is the AP threshold. Next, we plotted the membrane potential against its first derivative. The steepness of the AP (onset rapidity) corresponds to the slope of a line fit over three points starting at the threshold.

Postsynaptic excitatory currents recorded in voltage-clamp experiments were analyzed as follows: we smoothed the data with a 2.5-ms window and set the threshold to −10 pA. Parameters used in the find-peaks functions were: MinPeakHeight: −10 pA, MinPeakDistance: 0.5 ms, MinPeakProminence: 10 pA. We excluded data with a latency exceeding 25 ms and a duration of <10 ms. We further excluded neurons that did not respond reliably at 200 μA stimulus amplitude meaning responses with an amplitude of at least 100 μA in <60% of repetitions. EPSC rise time was defined as the time between response start and reaching 90% of the maximal amplitude. To determine the weighted decay time constant, we first fitted a double exponential fit (Eq. 1) to a 1-s range of the data starting at the time point of maximal amplitude and calculated the weighted decay time constant according to Equation 2. Fits with a goodness of fit (R^2) <0.95 were discarded.

$$A(t) = A_{slow} * exp\left(\frac{-t}{\tau_{slow}}\right) + A_{fast} * exp\left(\frac{-t}{\tau_{fast}}\right) \qquad (1)$$

$$\tau_w = \frac{(A_{slow} * \tau_{slow} + A_{fast} * \tau_{fast})}{(A_{slow} + A_{fast})}. \qquad (2)$$

Histology
In a subset of recorded cells, their identity was confirmed *post hoc*. Therefore, slices were fixed overnight in 4% paraformaldehyde [PFA in phosphate buffer solution (PB)], cryoprotected in 30% sucrose (in PB), resectioned to 80 μm and submitted to a diamino-benzidin (DAB) protocol (Niederleitner and Luksch, 2012). After the DAB-staining, sections were mounted onto chromalum gelatin-coated slides, dried overnight, counterstained with neutral red and coverslipped with DPX.

Only neurons were taken into account that were either directly confirmed to be SCN by injection of Lucifer yellow or DIOC16 or *post hoc* after biocytin injection.

Hybrid voltage sensor imaging (hVOS)
hVOS allows visualization of changes in membrane voltage with high temporal precision and a good signal-to-noise ratio (Chanda et al., 2005; Bradley et al., 2009; Weigel et al., 2014).

For hVOS, slices were incubated in aCSF containing 0.5 μM dipicryl-amine (DPA) for at least 45 min before the start of the experiment. Afterwards, slices were transferred to the working chamber under the microscope (AxioExaminer, Zeiss) and continuously perfused with oxygenated DPA-containing aCSF at RT. Extracellular electrical stimulation were performed the same way as in patch-clamp experiments.

To image the signal propagation SCNs were labeled with a lipophilic carbocyanine fluorescent dye [3,3'-dioctadecyloxa-carbocyanine perchlorate (DiO); 2 μM DiO dissolved in internal solution] via a patch-clamp pipette in cell-attached mode.

After sufficient labeling of the cell, DiO containing cells were illuminated via a LED with a peak wavelength of 457 nm (LZ4-00B208, LED Engin). The energy transfer from the electron donor (DiO) to the electron acceptor (DPA) results in a quenching of brightness that was detectable with a CCD camera system (NeuroCCD-SM256, RedShirtImaging; frame rate of 2 kHz at 80 × 80-pixel resolution (equivalent to ~380 × 380 μm) with Neuroplex software, version 9.3.0, RedShirtImaging). The combination of LED illumination and camera resolution limits the detection of signals in noise to pixels that are mostly covered by cellular structures. Thus, recording of fine structures (e.g., axons and dendrites) was not possible.

To analyze the signal propagation in SCNs data were processed with a custom-written script based on the data analysis procedure described by Hochbaum et al. (2014). Briefly, data were imported to MATLAB, the stimulation time points were detected, and data with a high level of baseline noise (ΔF/F >10%) was removed, as a high noise level were usually caused by moving particles or underexposed parts of the image that did not contain information. Afterwards, data were digitally filtered (10-Hz high-pass, bandstop-filter at 50, 100, and 220 Hz) and smoothed to remove shot noise by a 3-D Kernel ([0 1 0; 1 2 1; 0 1 0], [1 2 1; 2 4 2; 1 2 1], [0 1 0; 1 2 1; 0 1 0]). For further analyzing, the data points between 50 ms before and 250 ms after stimulus onset were extracted. The maximal activity of the recorded fluorescence signal in this range was plotted in an intensity plot to select a region of interest (ROI), which represented the soma. A normalized, 10-fold oversampled signal template was built based on the mean signal recorded at the ROI and events were detected by template matching. We generated a 10-fold oversampled data set used to analyze signal propagation. To determine the direction and

Table 1. Morphologic and physiological parameters of the different compartments of the SCN model

	Soma	Proximal basal dendrite	Distal basal dendrite	Primary neurite	Distal apical dendrite	Axon initial segment	Axon internode	Axon node
Diameter (µm)	20	2	2	3	2	3	2	2
Length (µm)	20	25	175	60	230	50	1000	3
g_{Leak} (S/cm^2)	0.0001	0.00001	0.00001	0.0001	0.0001	0.0001	$1*10^{-6}$	0.0001
g_{NaHH} (S/cm^2)	0.2	0	0	0.22	0	0.24	0	0.32
g_{KHH} (S/cm^2)	0.04	0	0	0.04	0	0.04	0	0.04
g_{KHT} (S/cm^2)	0.013	0.013	0	0.013	0	0.013	0	0
C_m (µF/cm^2)	1	1	1	1	1	1	0.01	1
R_a (Ω*cm)	150	150	150	150	150	150	150	150

velocity of signal spread, we evaluated these time points along an axis from apical to basal, plotted them against the distance and fitted the data linearly. The resulting slope is equivalent to the propagation velocity. A positive slope means a spread from apical to basal, a negative slope the opposite. For analysis of signal propagation, we only included data that we could average over at least 15 pixels ($\sim$75 µm).

Multicompartment model based on anatomic data
We created a multicompartment model based on the anatomic data published before (Lischka et al., 2018). For this, we used NEURON 7.8.2 (Hines and Carnevale, 1997, 2000, 2001; Hines et al., 2009) as a module in Python 3.8.10, all simulations were run under Ubuntu Server 20.04. The model consisted of a somatic compartment, a basal dendrite consisting of proximal and distal compartments. Opposite of the basal dendrite a primary neurite was connected to the soma. At the distal end of the primary neurite, an axon model and a distal apical dendrite were connected. The axon model consisted of an initial segment and two pairs of internode and node. The parameters of each compartment are given in Table 1. Reversal potentials were set to $E_K = -80$ mV and $E_{Na} = 50$ mV. See Figure 7A for a graphical overview of the model morphology. Whenever direct physiological data were unavailable, parameters were chosen for the model performance to closely match the *in vitro* recordings from SCN neurons in our own current-clamp and voltage-clamp experiments.

Synaptic inputs to the SCN model were represented by conductance point sources (NEURON *ExpSyn2* mechanism) that were either activated deterministically at a given point in time without random variations of individual onset (to simulate *in vitro* electrical stimulation) or stochastically by independent random spike trains generated with the NEURON *NetStim* mechanism. The *NetStim* mechanism produced random spike times with a negative exponential distribution of inter-event intervals. We simulated excitatory inputs in detail (N_{syn} = 25 per dendrite) using data from our own *in vitro* recordings. Accordingly, the apical excitatory inputs had slower kinetics (τ_{rise}: 3 ms, τ_{decay}: 80 ms) compared with basal excitatory inputs (τ_{rise}: 1.2 ms, τ_{decay}: 25 ms) while generating the same peak synaptic currents as the basal inputs (Σg_{syn}: 10 nS per side). Thus, NMDA contribution to resting EPSC was simplified to differences in decay time constant, disregarding potential voltage-dependent properties of NMDA channels. In some experiments, the τ_{decay} of apical synapses was reduced to 30 ms to simulate block of NMDA components. Excitatory inputs were distributed evenly over the distal apical and basal dendritic compartments and were simulated with a reversal potential of 0 mV.

The neuronal transduction of visual information to the tectum is lagging the auditory inputs by $\sim$30–60 ms depending on stimulus form (Schmidt and Bischof, 2001; Gutfreund et al., 2002; DeBello and Knudsen, 2004; Spitzer et al., 2004; Verhaal and Luksch, 2016a). In simulated *in vivo* experiments, we, therefore, imposed a modality-specific delay on the inputs, representing typical differential processing delays in the visual (50 ms) and the auditory (20 ms) pathways to the TeO.

For comparability, we chose the input rates for apical and basal connections to produce between 0 and 55 AP output on 125 ms of unimodal stimulation. To achieve this, apical inputs were driven at average rates between 35 and 70 Hz and basal inputs at rates between 75 and 333 Hz. A duration of 500 ms per repetition was used in most experiments at a

temporal resolution of 25 µs. In a few instances, a much higher temporal resolution (500 ns) was used to better observe the spread of excitation in the model. In these simulations, membrane voltage was simultaneously observed for many locations at 2-µm spatial intervals and AP maxima were detected and timed.

Inhibitory feedback is necessary for multimodal integration (Friedel and van Hemmen, 2008; Cuppini et al., 2010; Stein et al., 2014; Felch et al., 2016; Kardamakis et al., 2016; Miller et al., 2017). We included feedforward inhibition converging onto the SCN neuron in the model by placing a total of four conductance point sources (*ExpSyn* mechanism) on the distal dendritic compartments (at 0.4 compartment lengths; g_{syn}: 1 nS per synapse, τ_{decay}: 75 ms, E_{rev}: –85 mV). One inhibitory input on each distal dendrite was driven by the same average input rate at which the apical inputs were activated, one on each distal dendrite was driven by the average rate of basal input activation. An additional delay of 5 ms before activation of the feed-forward inhibition was imposed.

We measured V_m at the center of the second axon node and detected APs by their steep negative slopes. Peak AP times were collected and counted per repetition. In some experiments, we determined the voltage threshold of AP generation by thresholding the rate of rise of V_m in the phase plane. The response of the SCN model to a given condition was quantified as the mean $\pm$ SD of the number of AP in at least $n > 50$ repetitions (with varying but known random seeds).

We determined multimodal enhancement as the increase in average number of AP generated in the multimodal condition over the sum of APs generated in apical and basal unimodal conditions at the same input power. To simulate varying distance of stimulus sources to the virtual animal we increased the onset of basal auditory inputs by 1/343 s (the inverse of the speed of sound) for every meter of distance. This changed the temporal relation between the onset of the visually-driven and auditory-driven excitation at the level of the SCN. Thus, a specific set of effective visual (50-ms internal pathway delay) and auditory (20-ms internal pathway delay + variable external delay) onset latencies corresponded to a virtual distance from a multimodal sound source. In experiments concerning the SCN-specific properties of the model we gradually varied the length of the primary neurite between 0.1 and 125 µm and the contribution of NMDA-type glutamate receptors to apical excitatory synapse kinetics (apical τ_{decay} 20–120 ms) while keeping all other factors constant.

Code accessibility
Code used for data analysis will be provided on request. All code used for the NEURON model can be reviewed at https://github.com/thkupy/SCNv2.

Statistical analysis
Statistical analysis was performed with MATLAB or, in case of the model, with Python. Results are expressed as mean $\pm$ SEM or as mean $\pm$ SD (modeling data). Physiologic data derived from *in vitro* experiments were analyzed with non-parametric tests. In case of pairwise comparison, we used a two-sided Wilcoxon rank-sum test. Otherwise, a Kruskal–Wallis test with a Tukey–Kramer *post hoc* test was used. Statistical testing of modeling data was performed using ANOVA and *post hoc* pairwise *t* tests with Bonferroni correction for repeated testing.

The statistical analysis was conducted at 95% confidence level. $p <$ 0.05 was considered statistically significant.
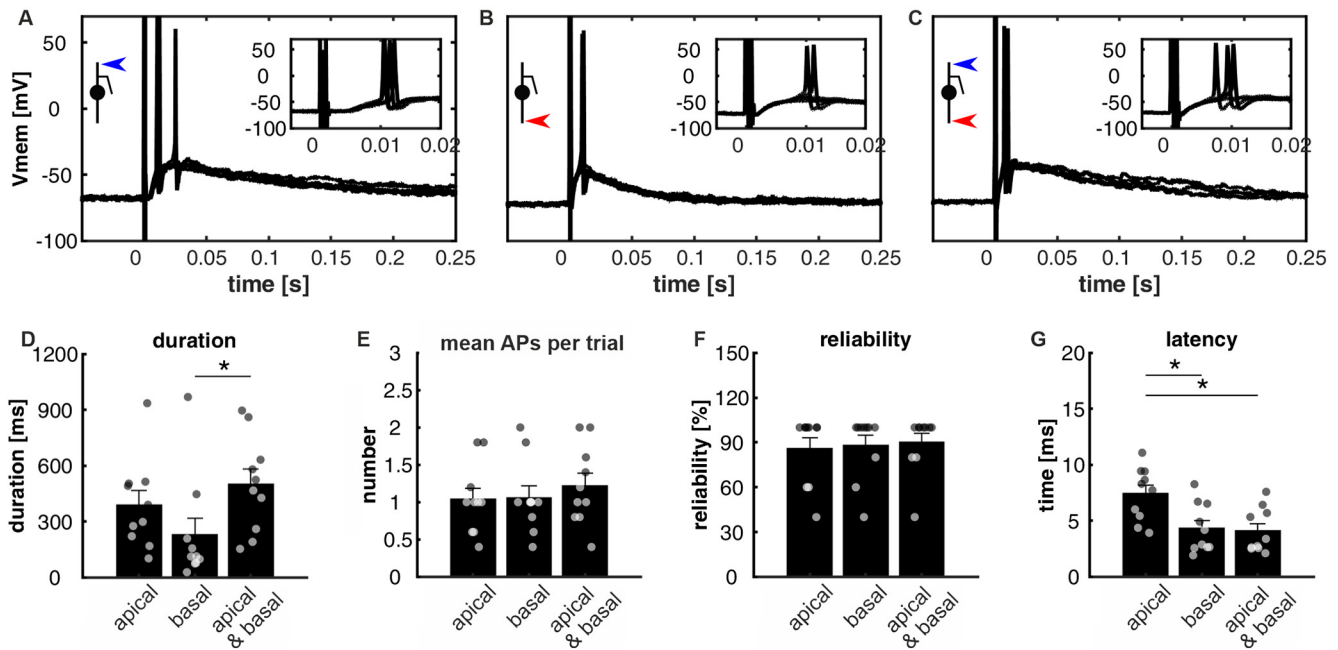
Figure 2. Unimodal suprathreshold activation of SCNs did not lead to significant bimodal enhancement. ***A–C***, Responses of an exemplary SCN to unimodal electrical stimulation in layer 1–4 (***A***), layer 13 (***B***), and simultaneous applied stimuli on both stimulation sites (***C***; each showing 5 repetitions). The insets show responses at higher temporal magnification to discriminate response and stimulus artifact. ***D–G***, Quantification of response parameters: duration (***D***), mean number of evoked APs per trial (***E***), reliability of evoked APs (***F***), and latency (signal first time above a threshold, ***G***). Bar plots show mean ± SEM ($n = 10$); asterisk indicate $p < 0.05$ (Kruskal–Wallis test with Tukey–Kramer *post hoc* test). Values of each neuron (mean of 5 repetitions) are plotted as dots on the corresponding bars.

Results

Electrophysiological properties of SCNs

We first examined the physiological properties of SCNs with whole-cell patch clamp experiments. We only considered cells that were clearly identified as SCN by their characteristic morphology with the axon originating at the primary dendrite in the form of a Shepherd's crook ($n = 27$; Fig. 1*A*). The neurons responded to depolarizing current steps either with a phasic response ($n = 16$; Fig. 1*Bi*) or with tonic firing ($n = 11$; Fig. 1*Bii*). Both response types differed significantly in their input resistance (Fig. 1*D*, phasic: 417 ± 45 MΩ, tonic: 832 ± 76 MΩ, $z = -3.8243$, $p = 0.0001$), in their resting membrane potential (Fig. 1*E*, phasic: −56.9 ± 2.0 mV, tonic: −49.6 ± 1.8 mV, $z = -2.4993$, $p = 0.0125$), maximal numbers of evoked APs (Fig. 1*F*, phasic: 1.9 ± 0.4, tonic 7.9 ± 1.2, $z = -4.0259$, $p = 0.0001$), the injected current necessary to evoke the first AP (Fig. 1*G*, phasic: 0.15 ± 0.03 nA, tonic: 0.03 ± 0.01 nA, $z = 3.4885$, $p = 0.0005$), the latencies of the first evoked AP (Fig. 1*H*, phasic: 13.7 ± 4.9 ms, tonic: 45.5 ± 9.4 ms, $z = -2.7387$, $p = 0.00617$) and their half width (Fig. 1*I*, phasic 0.65 ± 0.09 ms, tonic 1.15 ± 0.13 ms, $z = -2.7186$, $p = 0.0066$; two-sided Wilcoxon rank-sum test). Membrane time constants (Fig. 1*C*, phasic: 33.3 ± 5.1 ms, tonic: 28.3 ± 3.3 ms, $z = 0.51814$, $p = 0.6044$) and AP amplitude (Fig. 1*J*, phasic: 105.9 ± 4.9 mV, tonic: 106.1 ± 4.2 mV, $z = -0.07402$, $p = 0.9410$) were comparable. We successfully evoked APs by apical presynaptic electrical stimulation in 19 out of 27 neurons (phasic: $n = 10$, tonic $n = 9$) and basal presynaptic electrical stimulation in 11 out of 27 neurons (phasic: $n = 4$, tonic: $n = 7$). However, the amplitude of the external stimulation necessary to evoke postsynaptic APs differed broadly (10–300 pA).
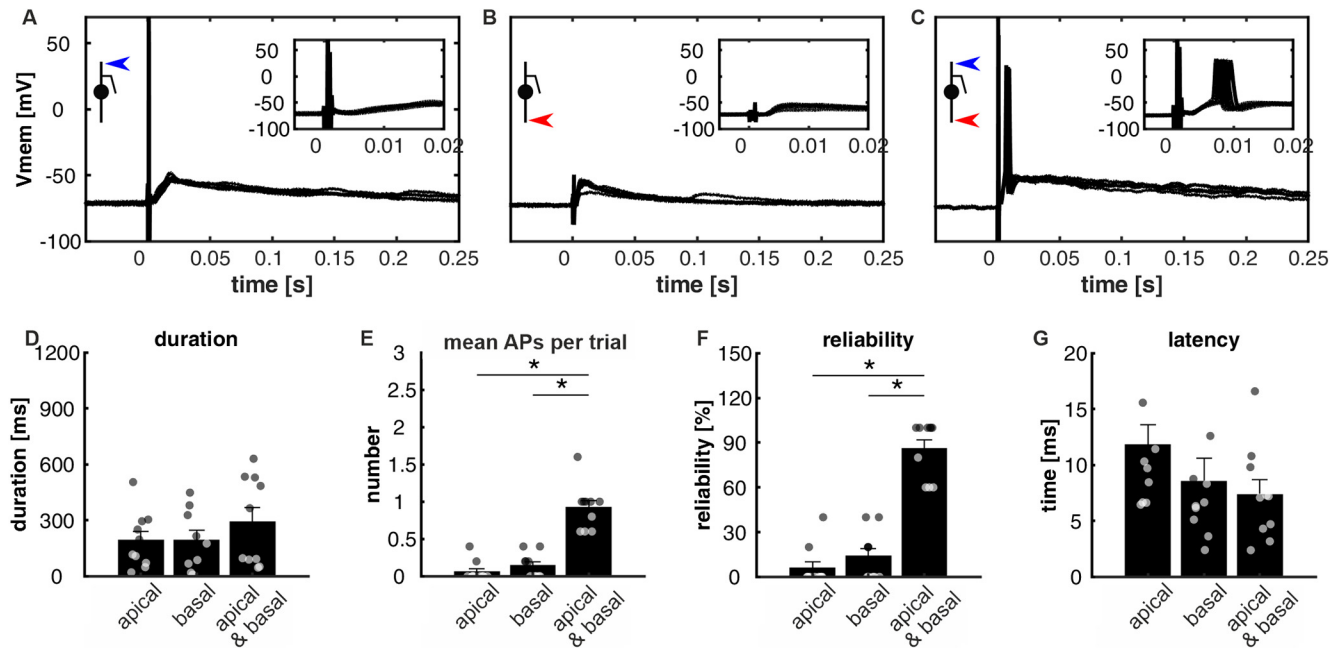
Bimodal stimulation enhances the response compared with unimodal stimulation

In the following, we will call electrical stimulation of either the apical or the basal layers of the TeO as "unimodal" and simultaneous stimulation as "bimodal." As both unimodal stimuli were sufficient to evoke APs, we studied how bimodal stimulation changed the cellular response ($n = 10$). First, we tested this for suprathreshold unimodal activation (Fig. 2*A–C*). Typically, extracellular stimulation evoked one to a few APs followed by a prolonged depolarization. The total duration was typically, but not significantly, longer in case of apical stimulation (390 ± 76 ms) compared with basal stimulation [229 ± 90 ms, $p = 0.1168$ (Fig. 2*D*); see also Fig. 3*A,B*, Kruskal–Wallis test]. The mean number of evoked APs per repetition were similar (Fig. 2*E*, apical: 1.04 ± 0.15, basal: 1.06 ± 0.16, $p = 0.9999$, Kruskal–Wallis test) and, thus, the reliability in the response (Fig. 2*F*, apical: 86 ± 7%, basal: 88 ± 7, $p = 0.9951$, Kruskal–Wallis test). However, the latency was significantly shorter in basal stimulation (Fig. 2*G*, apical: 7.4 ± 0.8 ms, basal 4.3 ± 0.7 ms, $p = 0.0320$, df = 2, $\chi^2 = 9.9019$, Kruskal–Wallis test).

Simultaneous activation of the dendrites evoked a response that combined the short latency of basal unimodal stimulation and the prolonged depolarization of apical unimodal stimulation (Fig. 2*C*). The increase in duration was significant compared with basal stimuli (Fig. 2*D–G*; duration: 500 ± 81 ms, $p = 0.7263$ to apical and $p = 0.0168$ to basal stimulation, df = 2, $\chi^2 = 8.0206$; latency: 4 ± 0.6 ms, $p = 0.0106$ to apical and $p = 0.9231$ to basal stimulation, df = 2. $\chi^2 = 9.9019$; mean number of evoked APs per trial: 1.22 ± 0.17, $p = 0.7293$ to apical and $p = 0.7213$ to basal stimulation, df = 2, $\chi^2 = 0.77783$; reliability: 90 ± 6% $p = 0.9806$ to apical and $p = 0.9951$ to basal stimulation, df = 2, $\chi^2 = 0.035474$; $n = 10$; all data tested for significance by Kruskal–Wallis tests). The shape of the AP was similar in all instances (AP half width, AP height, AP threshold, onset rapidity; data not shown) indicating a common origin.

The amount of enhancement in multimodal integration *in vivo* was shown to follow the rule of inverse effectiveness. Therefore, strong stimuli of different modalities will result in

Figure 3. Unimodal subthreshold activation of SCNs led to nonlinear multimodal enhancement. **A–C**, Responses of an exemplary SCN to subthreshold unimodal electrical stimulation in layer 1–4 (**A**), layer 13 (**B**), and simultaneous applied subthreshold stimuli on both stimulation electrodes (**C**; each showing five repetitions). The insets show responses at higher temporal magnification to discriminate response and stimulus artifact. **D–G**, Quantification of response parameters: duration (**D**), mean number of evoked APs per trial (**E**), reliability to evoke APs (**F**), and latencies (**G**). Bar plots show mean ± SEM (n = 10), asterisk indicate p < 0.05 (Kruskal–Wallis test with Tukey–Kramer *post hoc* test). Values of each neuron (mean of 5 repetitions) are plotted as dots on the corresponding bars.

only mild enhancement of cellular activity, if at all. However, weak sensory information should lead to a nonlinear, superenhanced response that increases the salience of an otherwise subthreshold stimulus. To simulate this in a slice preparation, we chose extracellular stimuli that were just below AP threshold (Fig. 3A,B, n = 10). However, each stimulus was able to robustly elicit postsynaptic, subthreshold potentials. EPSP duration was comparable between stimuli (Fig. 3D, apical: 192 ± 47 ms, basal: 192 ± 54, df = 2, χ^2 = 46.2222, p = 0.9662). Latencies were again slightly but not significantly shorter for basal stimuli (Fig. 3G, apical: 11.8 ± 1.8 ms, basal 8.5 ± 2.0 ms, df = 2, χ^2 = 4.0981; p = 0.1950). We only occasionally observed APs (Fig. 3E, mean number of evoked APs per trial: apical: 0.06 ± 0.04, basal: 0.14 ± 0.05, df = 2, χ^2 = 21.8517, p = 0.7203; Fig. 3F, reliability: apical: 6 ± 4%, basal 14 ± 5%, df = 2, χ^2 = 21.9321, p = 0.7194). In case of simultaneous subthreshold stimulation, the neurons responded with APs followed by a prolonged depolarization (Fig. 3C,E, duration: 292 ± 75 ms, p = 0.6779 to apical and p = 0.5341 to basal, df = 2, χ^2 = 1.2751). The response started with a latency comparable to basal stimulation (Fig. 3G, 7.3 ± 1.3 ms, p = 0.1770 to apical and p = 0.9986 to basal, df = 2, χ^2 = 4.0981) and was very reliable (Fig. 3E,F, mean number of evoked APs per trial: 0.9 ± 0.1, p < 0.0001 to apical and p = 0.0009 to basal stimulation, df = 2, χ^2 = 21.8517; reliability: 86% ± 6, p < 0.0001 to apical and p = 0.0009 to basal stimulation, df = 2, χ^2 = 21.9321; n = 10; all data tested for significance by Kruskal–Wallis tests).

Taken together, SCN responded to both apical (visual) and basal (auditory) dendritic synaptic input *in vitro*. Unimodal activation evoked subthreshold responses or APs. Bimodal stimulation enhanced the SCN responses compared with unimodal activation. The amount of enhancement was inversely correlated to the unimodal response strength. Thus, we conclude that in the brain this neuron type should be capable of passing on unimodal

information from both input modalities as well as integrate those inputs in a multimodal situation.

Dependency of unimodal responses on stimulus intensity
To understand the mechanism of signal integration and bidendritic enhancement, we studied postsynaptic currents evoked by unimodal stimulation of apical and basal dendrites in whole-cell voltage-clamp experiments. Therefore, we prevented interference with voltage-activated sodium channels by an intracellular block with QX314. Successful diffusion of QX314 was verified by elimination of somatically evoked APs, which was achieved in two to 5 min after break in.

Postsynaptic events will depend on the type and amount of presynaptically activated transmitter release, which correlates to the quality and strength of extracellularly applied electrical fields (Grill, 1999). Thus, in theory not only the amount of released transmitters from one population of neurons might increase with increasing stimulus strength, but also other neuron types (e.g., bypassing fibers) might be activated depending on stimulus size. Therefore, we tested the dependency of postsynaptic responses on stimulus intensity. We hypothesized a gradual change in response in case of activation of a homogenous population until a steady-state value or inconsistent responses in case of crosstalk between the dendrites or recruitment of heterogeneous neuronal populations.

Both apical and basal synaptic activation evoked postsynaptic currents recorded at the soma. Figure 4 is showing the EPSCs evoked by apical (A) and basal (B) stimuli of different amplitude [mean of five repetitions; color-coded: light gray (50 µA) to black (200 µA); insets are showing enlarged sections 10 ms before to 50 ms after stimulus onset]. Postsynaptic responses showed a dependency on stimulus strength: EPSC amplitude and duration increased (Fig. 4C,D) and the latency decreased (Fig. 4E) with increasing stimulus amplitude. Steady state values were usually
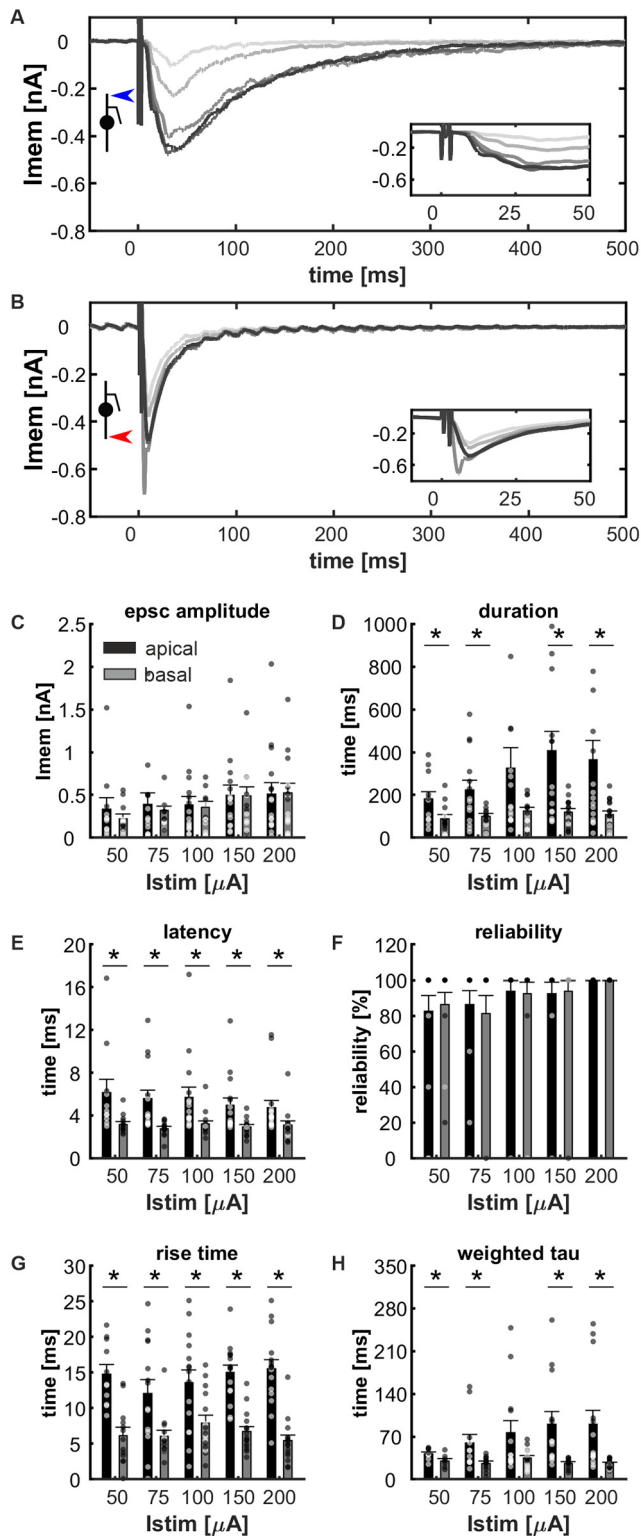
Figure 4. Dependency of postsynaptic response on stimulus amplitude. Exemplary voltage-clamp recordings of a neuron with intracellularly applied voltage-gated sodium channel blocker QX-314 show evoked postsynaptic currents to electrical pulses (50–200 µA) applied to layer 1–4 (**A**) or to layer 13 (**B**; stimulus paradigm indicated by blue or red arrow). Increasing gray values indicate stronger stimuli (light gray: 50 µA; black: 200 µA). **C–H**, Bar plots of EPSC amplitude (**C**), duration (**D**), latency (**E**), reliability (**F**), rise time (**G**), and weighted tau (**H**) in dependence of stimulus amplitude and stimulus location (black = apical stimulation, gray = basal stimulation). Data are plotted as mean ± SEM; $n = 16$, asterisk indicate $p < 0.05$ (two-sided Wilcoxon rank-sum test). Mean values of each neuron (5 repetitions) are plotted as dots on the corresponding bars.

reached at ∼100- to 150-µA stimulus amplitude indicating maximal recruitment of input fibers, which is also represented in a high response reliability at 100 µA and higher (Fig. 4F). However, we found a broad range of response amplitudes between neurons (e.g., 200 µA: apical 0.17–2.04 nA; basal 0.23–1.62 nA).

Comparing the responses to apical ($n = 16$) and basal ($n = 16$) stimuli in detail, differences or similarities between apically and basally evoked responses were stable over the whole range of stimulus intensities. The mean response amplitudes (Fig. 4C; apical vs basal 50 µA: 336 ± 128 vs 223 ± 51 pA, $z = 0.5794$, $p = 0.5623$; 75 µA: 391 ± 134 vs 318 ± 50 pA, $z = -0.5095$, $p = 0.6104$; 100 µA: 380 ± 102 vs $\pm 354 \pm 70$ pA, $z = -0.1659$, $p = 0.8682$; 150 µA: 497 ± 116 vs 489 ± 107 pA, $z = 0$, $p = 1.0$; 200 µA: 512 ± 130 vs 524 ± 114 pA, $z = -0.2827$, $p = 0.7774$; two-sided Wilcoxon rank-sum test) and response probabilities (Fig. 4F; 50 µA: $83 \pm 9\%$ vs $86 \pm 7\%$, $z = -0.0992$, $p = 0.9210$; 75 µA: $86 \pm 8\%$ vs $81 \pm 10\%$, $z = 0.1386$, $p = 0.8898$; 100 µA: $94 \pm 6\%$ vs $93 \pm 6\%$, $z = 0.5217$, $p = 0.6018$; 150 µA: $93 \pm 6\%$ vs $94 \pm 6\%$, $z = -0.5217$, $p = 0.6018$; 200 µA: $100 \pm 0\%$ vs $100 \pm 0\%$, $z = 0$, $p = 1$; two-sided Wilcoxon rank-sum test) were always similar.

However, EPSC dynamics were different. The stimulation of the apical dendrite evoked significantly longer postsynaptic currents (Fig. 4C; 50 µA: 180 ± 36 vs 89 ± 20 ms, $z = 2.0857$, $p = 0.0370$; 75 µA: 224 ± 46 vs 101 ± 13 ms, $z = 2.0138$, $p = 0.0440$; 100 µA: 326 ± 94 vs 125 ± 18 ms, $z = 1.7006$, $p = 0.0890$; 150 µA: 408 ± 89 vs 119 ± 16 ms, $z = 2.4472$, $p = 0.0144$; 200 µA: 366 ± 90 vs 108 ± 17 ms, $z = 2.4309$, $p = 0.0151$; two-sided Wilcoxon rank-sum test). The latencies to basal stimuli were always significantly shorter (Fig. 4E; 50 µA: 6.1 ± 1.2 vs 3.1 ± 0.3 ms, $z = 3.0726$, $p = 0.0021$; 75 µA: 5.6 ± 0.8 vs 2.8 ± 0.2 ms, $z = 3.6891$, $p = 0.0003$; 100 µA: 5.7 ± 1.0 vs 3.2 ± 0.3 ms, $z = 3.4050$, $p = 0.0006$; 150 µA: 5.0 ± 0.7 vs 2.9 ± 0.2 ms, $z = 3.2447$, $p = 0.0012$; 200 µA: 4.8 ± 0.7 vs 3.1 ± 0.4 ms, $z = 3.3945$, $p = 0.0007$; two-sided Wilcoxon rank-sum test). We further determined the rise time (Fig. 4G) and the weighted decay time constant (Fig. 4H). Similar to the other parameters, rise times and decay time constants reached a steady state value if stimulus amplitudes were 100–150 µA. Responses to basal stimulation had a steeper onset (Fig. 4G; 50 µA: 14.8 ± 1.3 vs 6.1 ± 1.2 ms, $z = 3.5349$, $p = 0.0004$; 75 µA: 12.0 ± 2.0 vs 6.0 ± 0.9 ms, $z = 2.4020$, $p = 0.0163$; 100 µA: 13.6 ± 1.8 vs 7.9 ± 1.1 ms, $z = 2.3228$, $p = 0.0202$; 150 µA: 15.0 ± 1.1 vs 6.7 ± 0.7 ms, $z = 4.2308$, $p = 0.0002$; 200 µA: 15.5 ± 1.3 vs 5.4 ± 0.8 ms, $z = 4.3154$, $p = 0.0001$; two-sided Wilcoxon rank-sum test) and a faster decay tau (Fig. 4H; 50 µA: 41.8 ± 3.3 vs 30.2 ± 3.8 ms, $z = 2.05$, $p = 0.0401$; 75 µA: 59.9 ± 13.8 vs 26.3 ± 3.3 ms, $z = 2.2595$, $p = 0.0239$; 100 µA: 76.4 ± 20.3 vs 35.1 ± 4.3 ms, $z = 1.4315$, $p = 0.1523$; 150 µA: 90.0 ± 20.5 vs 26.5 ± 2.1 ms, $z = 3.5385$, $p = 0.0004$; 200 µA: 89.8 ± 22.7 vs 26.0 ± 1.9 ms, $z = 3.4697$, $p = 0.0005$; two-sided Wilcoxon rank-sum test).

Summarizing the results, we conclude that we recruited more fibers or fostered the release of more synaptic vesicles by increasing stimulus strength. However, apical versus basal electrical stimulation *in vitro* activated distinct homogeneous populations of presynaptic fibers.

The major excitatory neurotransmitter in the TeO is glutamate (Dye and Karten, 1996; Pires and Britto, 1997; Weigel and Luksch, 2012). Synaptic activation to SCNs can be blocked by 5 µM NBQX (Fig. 5A & B, inset; $n = 4$). Further, an involvement of NMDA-receptors in multisensory enhancement was demonstrated (Binns and Salt, 1996; Truszkowski et al., 2017). We hypothesized that NMDARs might cause the differences in
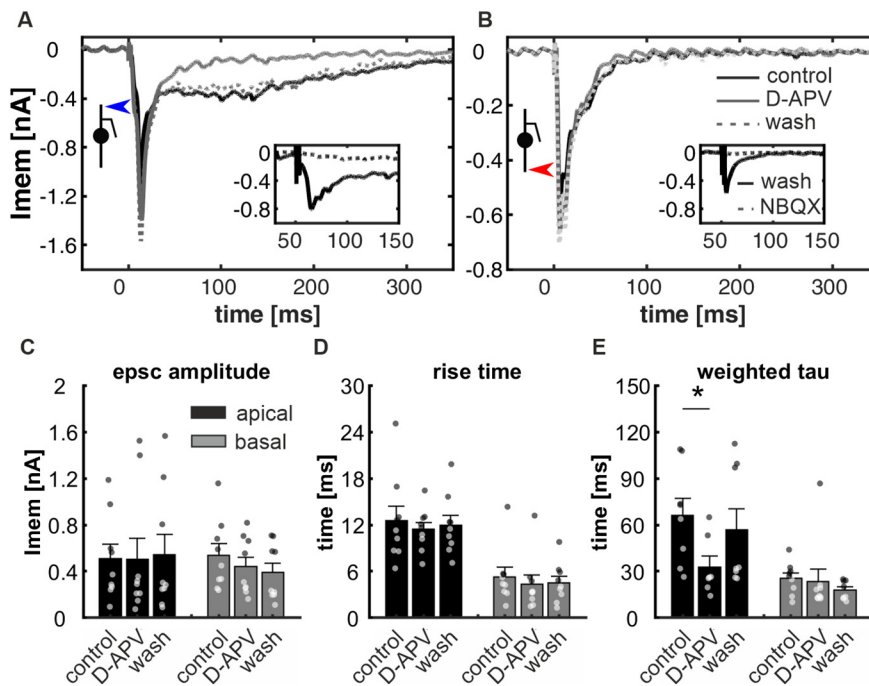
Figure 5. Effect of NMDAR antagonist D-APV on postsynaptic currents. Exemplary voltage-clamp recordings of a neuron with intracellularly applied voltage-gated sodium channel blocker QX-314 showing evoked postsynaptic currents to electrical pulses (mean of five repetitions, constant stimulus intensity) applied to layer 1–4 (**A**) or to layer 13 (**B**; stimulus paradigm indicated by blue or red arrow). Neurons were stimulated under control conditions (black line), application of D-APV for 15 min (light gray line) or after wash out for 15 min (dotted line). Insets **A**, **B**, Block of synaptically evoked potentials by NBQX application (dotted line) following the wash-out of D-APV (black line, $n = 4$). **C–E**, Bar plots of EPSC amplitude (**C**), rise time (**D**), and weighted tau (**E**) in dependence of pharmacological condition and stimulus location (black = apical stimulation, gray = basal stimulation). Data are plotted as mean ± SEM; $n = 9$, asterisk indicate $p < 0.05$ (Kruskal–Wallis test with Tukey–Kramer *post hoc* test). Mean values of each neuron (5 repetitions) are plotted as dots on the corresponding bars.

response between apical and basal activation and blocked NMDARs by 25 μM D-APV ($n = 9$). Figure 5 demonstrates the drastic impact mainly on the EPSC evoked by apical stimulation (Fig. 5A) and only minor effects on the EPSC evoked by basal stimulation (Fig. 5B). The response amplitude was only slightly and not significantly affected [Fig. 5C, apical before: 510 ± 121 pA, D-APV: 507 ± 183 pA, wash out: 542 ± 176 pA, df = 2, $\chi^2 = 0.3633$, $p = 0.8234$ (before to D-APV), 0.9211 (before to wash-out), 0.9765 (D-APV to wash out); basal before: 537 ± 101 pA, D-APV: 440 ± 81 pA, wash out: 391 ± 81 pA, df = 2, $\chi^2 = 2.2046$, $p = 0.7382$ (before to D-APV), 0.2982 (before to wash-out), 0.7382 (D-APV to wash out); Kruskal–Wallis test]. Also the rise time was not affected [Fig. 5D, apical before: 12.6 ± 1.9 ms, D-APV: 11.4 ± 0.9 ms, wash out: 12.0 ± 1.3 ms, df = 2, $\chi^2 = 0.0026$, $p = 1.0$ (before to D-APV), 0.9989 (before to washout), 0.9989 (D-APV to wash out); basal before: 5.3 ± 1.2 ms, D-APV: 4.3 ± 1.2 ms, wash out: 4.5 ± 0.9 ms; df = 2, $\chi^2 = 1.3165$, $p = 0.4963$ (before to D-APV), 0.9211 (before to washout), 0.7381 (D-APV to wash out); Kruskal–Wallis test]. The decay time constants of apically evoked EPSCs were mostly affected by NMDAR block. D-APV reduced the decay time constant nearly to the level of basal EPSCs [Fig. 5E, apical before: 66.3 ± 11.1 ms, D-APV: 32.9 ± 5.2 ms, wash out: 56.9 ± 13.6 ms, df = 2, $\chi^2 = 7.3051$, $p = 0.0455$ (before to D-APV), 0.6962 (before to wash-out), 0.2467 (D-APV to wash out); basal before: 25.6 ± 3.4 ms, D-APV: 23.5 ± 8.0 ms, wash out: 17.9 ± 2.1 ms; df = 2, $\chi^2 = 4.2363$, $p = 0.1738$ (before to D-APV), 0.2079 (before to wash-out), 0.9991 (D-APV to wash out); Kruskal–Wallis test].

While these data point toward differences in postsynaptic glutamate receptors between both dendrites, the particular

morphology of SCNs might lead to different control of the dendrites in voltage-clamp experiments because of space-clamp problems. To address this problem, we performed additional experiments in magnesium free aCSF (1 mM MgCl$_2$ substituted by 1 mM CaCl$_2$). While we saw a general increase in postsynaptic activity under these conditions, the postsynaptic current dynamics between presynaptic stimulation apical and basal to the SCNs were still significantly different [rise time: apical 34 ± 3 vs basal 14 ± 4 ms, z = 2.8318, $p = 0.0046$; decay time (weighted tau): apical 296 ± 28 vs basal 195 ± 28 ms, z = 2.5541, $p = 0.0106$, $n = 12$ apical, $n = 11$ basal, Wilcoxon rank-sum test]. We thus conclude that both dendrites indeed exhibited a different ratio of glutamate receptor subtypes.

Taken together, SCNs receive excitatory synaptic inputs on both apical and basal dendrites. Apical synaptic activation was slower and led to prolonged responses. The differences between apical and basal responses were caused by different NMDAR involvement on the different axodendritic domains.

Actions potentials are propagated from apical to basal independent of stimulation site

Given the separation of sensory input onto dendritic areas with different composition of glutamatergic receptors, the area at which integration and AP generation occurs is an important factor for understanding cellular computation in SCNs. Anatomical data suggest that APs are generated at the axon origin, which is located remote from the soma at the apical dendrite (Ramón y Cajal, 1909; Lischka et al., 2018). Our patch clamp data also suggested a common origin of AP generation. In order to test this further, we measured the spread of evoked APs in the cell after apical and basal stimulation with hVOS. It has to be mentioned that the detection of signal over noise by our particular setup is limited to larger cellular elements (e.g., soma and nearby larger neurites) as indicated in Figure 6A, upper left subplot.

Figure 6A–F shows the signal spread in an exemplary SCN. We aligned evoked events by their peak, which was determined by averaging the signal of all pixels with a signal over noise level and plotted the normalized amplitude as a false-color plot at different time points starting 1.5 ms before the peak until 1.5 ms after the peak (red = high and blue = low amplitude). Independent of stimulation site, we observed the activity peak apically before it shifted toward basal aspects (Fig. 6A–C; averaged APs: $n = 5$ apical stimulation (A), $n = 6$ basal stimulation (B), $n = 19$ simultaneous stimulation (C)). We quantified the spread by determining the time point of occurrence of the peak amplitude for each pixel (Fig. 6D1,E1,F1, plotted here as false-color plot, blue = early and red = late occurrence) and comparing this along the longitudinal axis of the neuron (Fig. 6D2,E2,F2). The slope of a line fit to the data is equivalent to the propagation velocity. Positive values represent a spread from apical to basal. We always found directionality from apical to basal ($n = 7$ for apical stimulation; $n = 10$ for
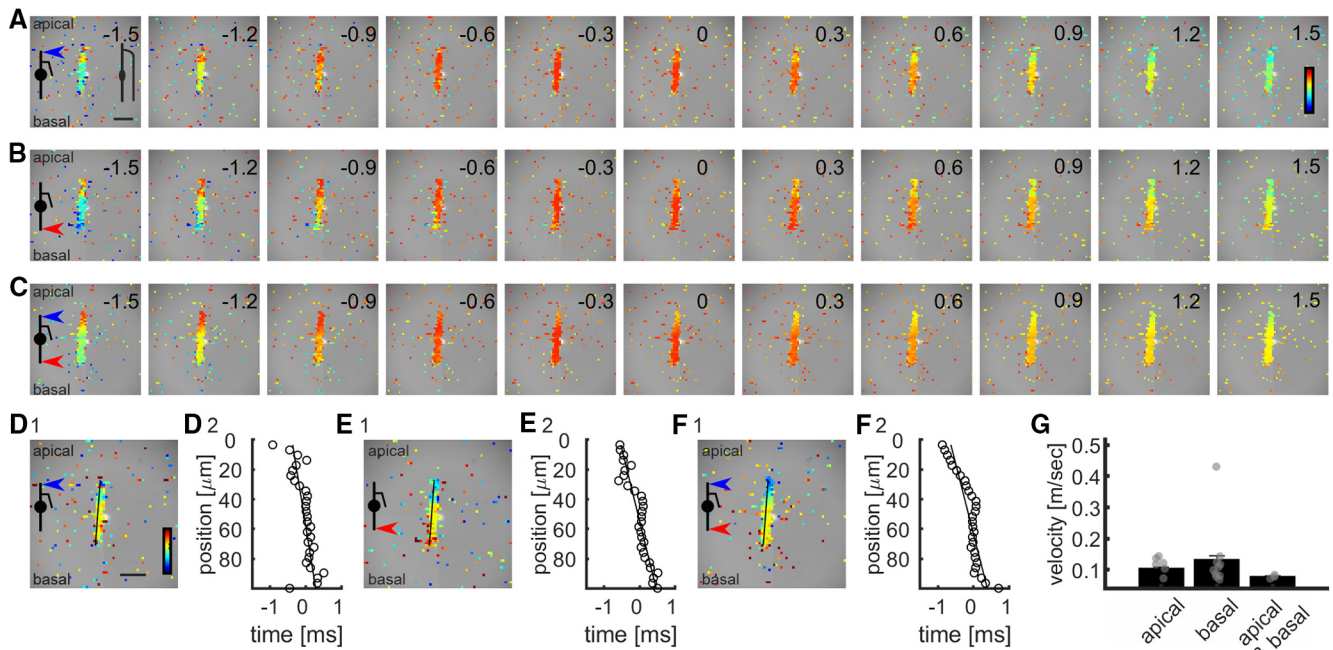
Figure 6. Signal propagation in SCNs. **A–C**, False-color plots of the normalized response of SCN to apical (**A**), basal (**B**), and simultaneous stimulation (**C**) at different time points (upper right corner of each subplot) relative to the mean peak-amplitude (apical $n = 5$, basal $n = 6$, and simultaneous $n = 19$). APs were peak-aligned to the mean signal form averaged over all pixels exhibiting a signal higher than noise. Schematics in the left panels (left) show the stimulus condition. The second schematic in **A**, left panel, depicts the probable recording area (without axon). Scale bar: 50 μm; color bar: 0 (blue) to 1.2 (red). **D1–F1**, False-color plot of the temporal occurrence of the signal maximum at different pixels relative to the mean peak-amplitude (**D1**: apical, **E1**: basal, **F1**: simultaneous stimulation; color bar: −1.5–1 ms; scale bar: 50 μm) and plot of the corresponding data derived from pixels (mean of three pixels in *Y* and *X* direction) along the longitudinal axis of SCN (**D2–F2**; axis marked in **D1–F1**). The slope of the fitted line is equivalent to the propagation velocity. A positive propagation velocity represents a spread from apical to basal. **G**, Summary of the propagation velocity for several neurons (apical: $n = 7$, basal: $n = 10$, simultaneous: $n = 3$). Data are plotted as mean ± SEM and were tested for significance by a Kruskal–Wallis test with Tukey–Kramer *post hoc* test.

basal stimulation; $n = 3$ for simultaneous stimulation). The propagation velocity was similar for all stimulation paradigms (Fig. 6G; apical: 0.10 ± 0.04 m/s, $n = 7$; basal: 0.13 ± 0.1 m/s, $n = 10$, simultaneous: 0.08 ± 0.005 m/s, $n = 3$, apical vs basal $p = 0.9952$, apical vs simultaneous $p = 0.2772$, basal vs simultaneous $p = 0.2758$, df = 2, $\chi^2 = 2.7$, Kruskal–Wallis test). Thus, our imaging data support the proposition that the site of AP initiation in these neurons is the axon emerging from the apical dendrite.

Multicompartment model demonstrates an effect of NMDAR contribution and morphology on multimodal integration

In order to better understand the principles of multimodal integration in SCN and to explore the role of the specific cellular features we next created a simplified multicompartment model based on anatomic SCN data published before (Lischka et al., 2018). The model SCN (Fig. 7A) consisted of a somatic compartment, and an apical primary neurite to which an axon initial segment and axon representation (consisting of two internode-node pairs) was connected. Following the immunohistochemical staining data from Lischka et al. (2018) these compartments contained voltage-activated sodium channels and high-voltage-activated potassium channels. Inhibitory feedforward connections were included in the model that were activated at the same modality-specific average input rates as the excitatory inputs. Because of the scarcity of physiological or ultrastructural data on the synaptic inputs connected to the apical and basal dendritic compartments, we modeled the input to SCN to match our own *in vitro* recordings as close as possible. Thus, when deterministically activated, both apical (Fig. 7B) and basal (Fig. 7C) inputs alone could cause reliable AP generation. However, on activation

of apical inputs the minimal conductance threshold (4.8 nS apical vs 5.4 nS basal) was lower for apical inputs compared with basal inputs (Fig. 7E). The higher efficacy of apical inputs was to a certain extent caused by the slower kinetics of apical inputs, as changing apical decay-tau to lower values in our simulations shifted the conductance threshold considerably to 5.1 nS (Fig. 7E). Not surprisingly, simultaneous activation of apical and basal inputs causes even more robust AP generation (Fig. 7D). Total synaptic conductance (apical + basal conductance combined) necessary for AP generation was only marginally lower for simultaneous activation compared with apical only activation (4.7 vs 4.8 nS); however, voltage threshold for AP generation in the simultaneous condition was consistently least depolarized (Fig. 7E). The site of AP initiation in the SCN model was always located in the primary neurite compartment (Fig. 7F). However, temporal differences of peak excitation along the length of the primary neurite were at least 10 times smaller than observed in our imaging experiments (compare Fig. 6) and the exact site of initiation depended on the ratio of apical to basal input conductance. Thus, the details of spatial AP initiation and spread of excitation differed slightly between our model and the real SCN. Nevertheless, we concluded from our initial simulations that apical excitatory inputs to SCN were much more effective than basal inputs, which was at least partially caused by their slower decay kinetics in addition to their privileged position close to the axon initial segment. However, the SCN model cell was most effectively driven by simultaneous activation of apical and basal inputs.

We then explored how stochastically activated apical and basal synaptic inputs representing presynaptic activity could drive the output spiking activity of the SCN model and how the
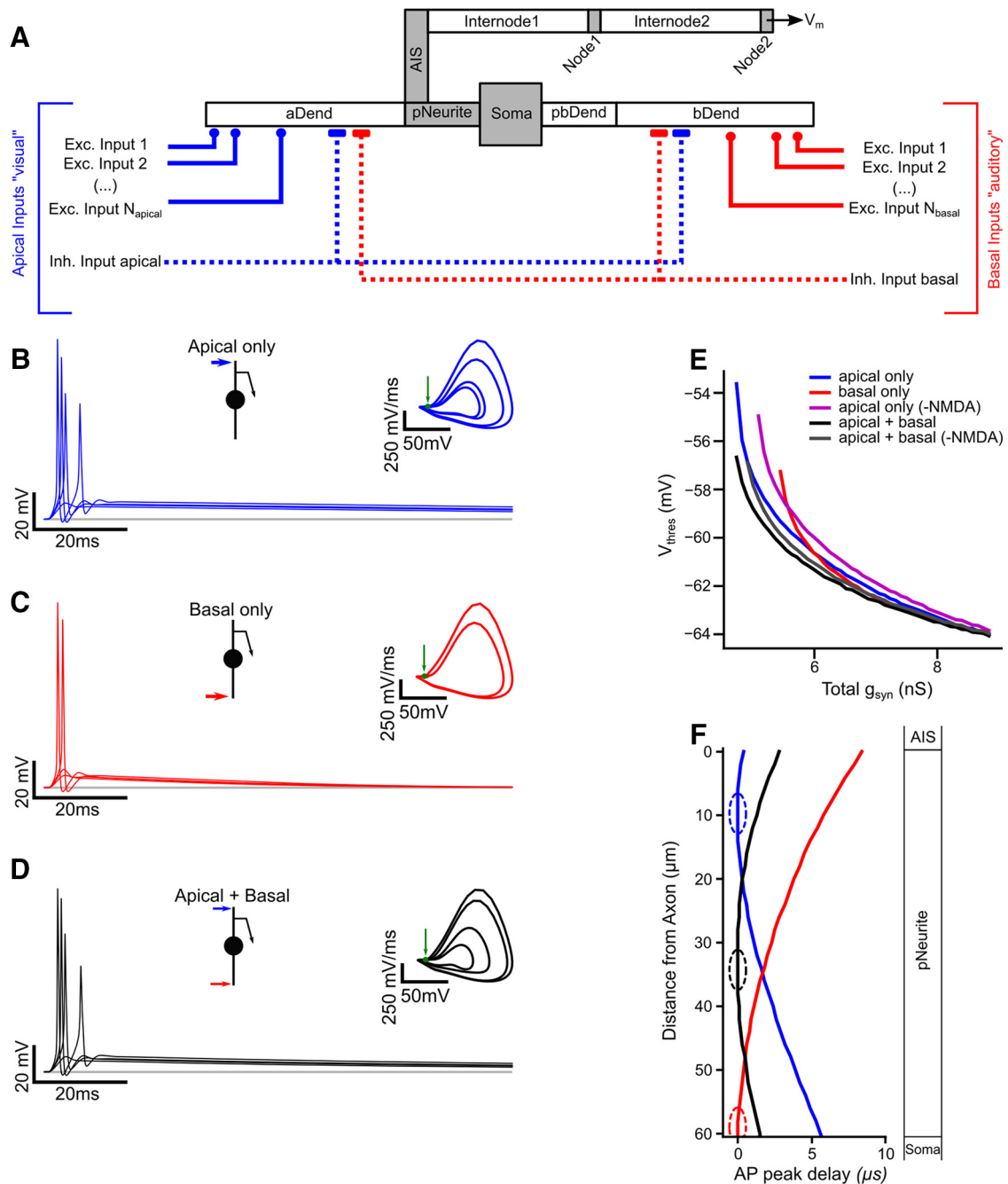
Figure 7. Performance of the SCN model in simulated *in vitro* experiments. **A**, Cartoon of the SCN model generated in NEURON. Blue lines indicate apical, visual connectivity. Red lines indicate basal, auditory connectivity. Dashed lines indicate inhibitory connections. aDend = distal apical dendrite; pNeurite = primary neurite; AIS = axon initial segment; Vm = measurement of the membrane potential; pbDend = proximal basal dendrite; bDend = distal basal dendrite. **B–D**, Simulated current-clamp responses on deterministic activation of apical (**B**), basal (**C**), and simultaneous apical + basal (**D**) excitatory inputs, as indicated by the inset depictions of the SCN. Simulations shown here run without feed-forward inhibition. Inset plots show phase-plane plots of the rate of change of V_m versus V_m. Green arrows in phase-plane plots indicate threshold rate at which AP generation was detected. **E**, Voltage threshold of AP activation, as determined from the phase-plane plots in **B–D**, plotted against total synaptic conductance g_{syn}. For "apical," "basal," and "apical/-NMDA" conditions, the total g_{syn} was distributed over $N = 25$ apical or $N = 25$ basal synapses. For the multimodal conditions ("apical+basal," "apical+basal/-NMDA") g_{syn} was distributed over $N = 25$ apical + $N = 25$ basal → $N = 50$ synaptic contacts. **F**, Time of maximal membrane potential deflection for "apical" (blue), "basal" (red), and "apical+basal" (black) activation of inputs, normalized to the time of first maximal potential deflection, plotted against spatial position on the primary neurite compartment. Dashed circles mark the location with minimal time delay of maximal membrane potential deflection, i.e., the site of impulse initiation.

simulated modalities interacted in these conditions (Fig. 8). This approach aimed to simulate virtual *in vivo* experiments, thus we included realistic neuronal pathways delays for visual (50 ms) and auditory (20 ms), reflecting the different amount of processing in the two sensory pathways leading up to the TeO. Upon stochastic activation of $N = 25$ apical inputs (Fig. 8A) the SCN

model robustly produced output spikes (Fig. 8A1,A2), albeit with a considerable average first spike latency (Fig. 8A3). This was only partially because of the longer simulated pathway delay. Instead, the shallower buildup of the postsynaptic response caused by the slower rise kinetics of apical inputs played a major role in these more delayed responses. Activation on average
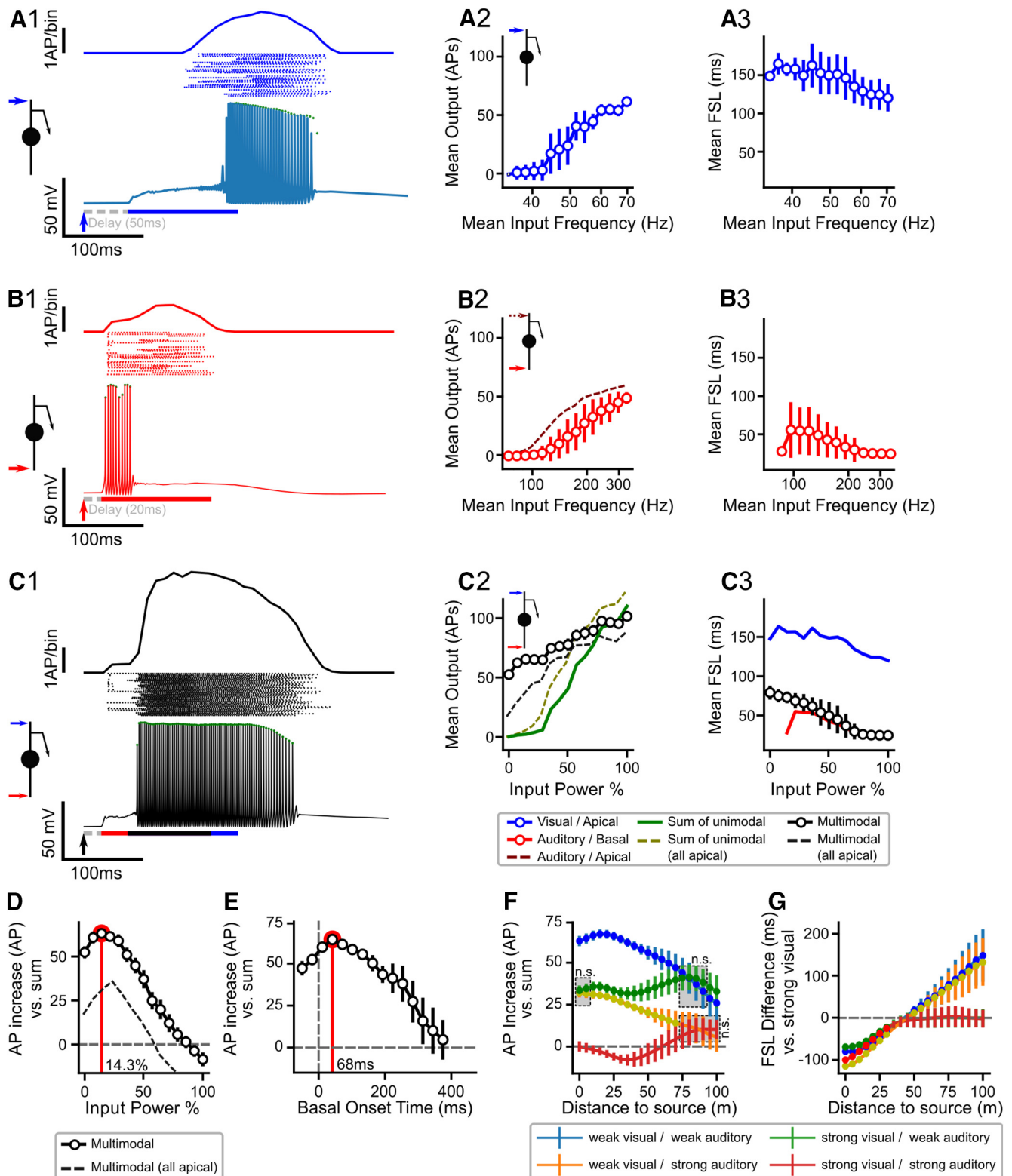
Figure 8. Superadditive multimodal enhancement with inverse effectiveness shown in the SCN model. *A–C*, For apical (*A*), basal (*B*), and multimodal (*C*) stochastic activation of inputs the responses to 125 ms stimulations are shown. Onset of virtual stimuli are marked with arrow (=0 ms), virtual pathway delay (visual: 50 ms; auditory: 20 ms) depicted by dashed gray bar, effective stimulus duration at level of the simulated cell shown by horizontal bars (visual: blue; auditory: red; multimodal: black). A single exemplary V_m trace (lower part of *A1–C1*), a rasterplot showing spike-times from *n* = 50 repetitions (middle part of *A1–C1*) and a peristimulus time histogram of the responses (upper part of *A1–C1*) is shown. Mean ± SD number of AP generated (*A2–C2*) and the mean ± SD first-spike latency (*A3–C3*) for the range of input rates we chose are shown. Dashed line in *B2*: data resimulated with basal synapses located at the apical dendrite. Dashed black line in *C2*: multimodal response with all synapses located at apical dendrite. Green line in *C2* indicates the sum of unimodal responses from *A2*, *B2*. Dashed green line in *C2* indicates sum of unimodal responses with all synapses located at apical dendrite. Blue and red lines in *C3* are mean first spike latencies replotted from *A3*, *B3* for comparison. *D*, Quantification of the multimodal enhancement in increase of the mean ± SD number of AP over the sum of unimodal responses versus input power (i.e., percentage of the range of input rates we chose). Gray dashed line indicates no enhancement (multimodal = sum of unimodal), red circle and vertical line marks condition of maximal enhancement. Dashed black line,

resulted in a bell-shaped peristimulus time histogram. Unimodal activation of basal inputs on the other hand resulted in briefer bursts of AP (Fig. 8B1,B2) with much shorter average first-spike latency (Fig. 8B3). On average, unimodal activation of basal inputs resulted in a similar peristimulus time histogram shape that was, however, more closely aligned with onset of the stimulus. When basal connections were relocated to the apical dendrite without changing parameters of input rate or synaptic properties, output spike rates were higher, which suggested that synapses on the apical dendrite drive outputs more efficiently (Fig. 8B2, dashed line). Multimodal stimulation of apical and basal inputs caused very robust, high-rate responses of the SCN model (Fig. 8C1,C2) with first-spike latencies (Fig. 8C3) that closely matched those observed in unimodal basal activation (compare Fig. 8B3). The shape of the peristimulus time histogram for multimodal stimulation was much more skewed toward the onset of the stimulus. AP output rates of multimodal stimulation were consistently superadditive compared with the sum of the unimodal responses at the same input power (Fig. 8C2) except at higher input powers: only at 86% and higher input power multimodal response rate became equal or less than the sum of unimodal responses (96 AP). When we connected both apical and basal synapses to the apical dendrite (Fig. 8C2, dashed lines) response rates were lower than in the regular case and only superadditive compared with the sum of unimodal responses for lower input rates (multimodal = sum of unimodal at 53% input power, 71 AP).

We quantified the increase of the number of AP of the multimodal versus the sum of the unimodal conditions (Fig. 8D) and found that weak input powers (here, 14.3% of the range used) resulted in highest benefits of the multimodal over the unimodal conditions (+63 AP compared with sum of unimodal). At highest input powers (>88% input power), multimodal AP count in fact became subadditive. Thus, multimodal responses of the SCN model were mostly superadditive and showed clear inverse effectiveness.

To highlight the role of the morphology of the SCN model, we again analyzed the increase of multimodal responses over the sum of unimodal responses when all input synapses were connected to the apical dendrite (Fig. 8D, dashed line). Here, maximal multimodal enhancement (+21 AP compared with the sum of unimodal) occurred at higher input power (35%) and became subadditive at much lower input powers (>53% input power).

←

Quantification of multimodal enhancement of responses with all synapses located at the apical dendrite. **E**, Temporal interaction window of apical and basal inputs quantified as the amount of enhancement at 20% input power (visual: 41 Hz; auditory: 103 Hz) for different basal onset times relative to a fixed apical onset time. Gray dashed lines indicate 0 s and no enhancement (as in **D**), red marker and vertical line indicate relative basal onset time with maximal enhancement. **F**, Enhancement quantified as the increase of the mean ± SD number of AP over sum of unimodal responses for different distances to the virtual stimulus source in meter, for different combinations of input powers: blue = weak visual/weak auditory; green = strong visual/weak auditory; orange = weak visual/strong auditory; red = strong visual/strong auditory. Input powers were: weak visual = 41.0 Hz, strong visual = 60.0 Hz, weak auditory = 103.0 Hz, strong auditory = 300.0 Hz. Circular markers indicate conditions where responses are significantly different (ANOVA and Bonferroni-corrected *post hoc t* test) from the strong/strong condition. Dashed gray areas mark conditions not significantly different from each other (see text). **G**, Mean ± SD of first-spike latencies for different distances to the virtual stimulus source in meter for different combinations of input powers, expressed relative to strong visual unimodal mean first spike latency. Presentation as in **F** except circular markers here indicate conditions where mean first spike latencies are significantly different (ANOVA and Bonferroni-corrected *post hoc t* test) from the strong visual unimodal condition.

Thus, in the SCN model the spatial separation of input modalities onto opposing dendrites increased the efficacy of multimodal enhancement and greatly expanded the effective input range over which it remained superadditive.

We next asked how the temporal relation between apical and basal inputs influence this result. For this, we kept the apical/visual onset constant and varied the basal/auditory onset time. Note that the realistic neuronal pathway delays are still included in this analysis, thus the basal onset time relates to the virtual stimulus onset (i.e., Fig. 8A1–C1, arrows), not the onset of excitatory activity at the level of the SCN (i.e., Fig. 8A1–C1, bars). Weak inputs at 25% power were used. A wide interaction window resulted from this (Fig. 8E). However, greatest enhancement occurred when basal inputs followed apical input onsets by 68 ms. When basal inputs followed apical inputs by >350 ms no enhancement was seen, thus indicating the end of the interaction window of two 125-ms stimuli.

An alternative approach to analyzing the temporal properties of the multimodal interaction in the SCN model was to express the relative onset times of apical and basal inputs as the distance to a virtual stimulus source. Given simultaneous onset of a multimodal stimulus at a remote source, auditory stimuli only will be subjected to an additional external delay on top of the differential internal pathway delays caused by the comparatively slow speed of sound. Thus, distance to multimodal sources will systematically change the temporal relation of inputs at the level of SCN. To explore this, we imposed an extra 1/343 s external delay (inverse of the speed of sound) per meter distance to the auditory stimulus and observed again the increased response on multimodal stimulation over the sum of unimodal inputs (as in Fig. 8D). This analysis is shown in Figure 8F. In addition, we were interested in the effect of the relative input power of the different modalities. As was already suggested from the results in Figure 8D, a weak visual and a weak auditory stimulus showed a much greater benefit from multimodal interaction than two strong stimuli. For this, we considered weak and strong stimuli that produce comparable unimodal output at the low and high end of the dynamic range respectively (weak visual = 41.0 Hz, strong visual = 60.0 Hz, weak auditory = 103.0 Hz, strong auditory = 300.0 Hz). The amount of enhancement for two weak multimodal stimuli declined with distance to the virtual stimulus (Fig. 8F) after showing a maximum at 20 m (corresponding to 58 ms additional delay). Interaction of weak or strong visual with weak or strong auditory stimulation produced intermediate enhancement at close range (for 0 m: ANOVA $F = 574$, df = 399, $p < 1e-6$; *post hoc* vs strong/strong: weak/weak: $T = 370$, $p < 1e-6$, weak/strong: $T = 210$, $p < 1e-6$, strong/weak: $T = 197$, $p < 1e-6$; weak/strong vs strong/weak: $T = 1.2$, $p = 0.22$). These conditions diverged with distance: while pairing a strong visual with a weak auditory stimulus became statistically indistinguishable from the weak/weak condition with range, enhancement of a weak visual with a strong auditory stimulus became absent for distances above 70 m (for 75 m: ANOVA $F = 242$, df = 399, $p < 1e-6$; *post hoc* strong/weak vs weak/weak: $T = 2.2$, $p = 0.28$; weak/strong vs strong/strong: $T = 2.59$, $p = 0.012$). At distances above 90 m, the condition with a strong visual and weak auditory stimulus actually showed greatest multimodal enhancement. Overall, these simulations suggested that the actual amount of multimodal benefit depended on the distance to the stimulus source and the relative power or salience of the stimuli involved.

Apart from the enhancement of AP rate (Fig. 8C3) we showed that the average first-spike latency of multimodal stimuli was strongly affected. We thus asked how much faster a multimodal stimulus would cause significant AP activity compared with a strong visual stimulus alone. Obviously (compare Fig. 8A–C), multimodal responses cannot be faster than the fastest auditory responses. However, as the TeO is a predominantly visual brain structure, it appeared opportune to compare the unimodal response latency of the main modality to those of multimodal conditions. It became obvious (Fig. 8G) that for distances below 35 m, all multimodal stimuli, regardless of their input power, had significantly lower first-spike latencies than visual stimuli alone. Here, weak visual paired with strong auditory stimuli showed the greatest increase in average first-spike latency: −124 ± 1 ms.

In the next set of experiments, we tried to better understand the impact of the cellular peculiarities of the SCN on multimodal enhancement. The modeling approach provides unique opportunities to accomplish this. To this end, we repeatedly simulated data as in Figure 8D while systematically varying the length of the primary neurite between 0.1 and 125 µm (Fig. 9). Further, we systematically varied the decay time constant of the apical excitatory inputs between 20 and 120 ms as a first order approximation of the contribution of NMDA type glutamate receptors to the resting EPSC (Fig. 9F–J). These simulations allowed a quantitative prediction of the influence that cellular and physiological properties of SCN had on multimodal processing.

The length of the primary neurite (pNeurite) had a strong inverse impact of the efficacy on the apical (Fig. 9A), and to a somewhat lesser degree on the basal (Fig. 9B), excitatory inputs, as was evident from the unimodal response rates. For a given pNeurite length, increasing unimodal input power increased SCN output rates. However, the input-output relation strongly depended on the pNeurite length, with shorter pNeurite causing higher maximal unimodal output rates for the input range used in these simulations and, in consequence, a steeper dynamic output range. Accordingly, the multimodal response rates (Fig. 9C) also increased with decreasing pNeurite length. Again, maximal output rates on the range of input rates and the slope of the dynamic range depended on pNeurite length. Compared with this, the sum of unimodal response rates (Fig. 9D) was generally very low for (<10 AP) for weak stimuli but showed similar maximal sum of output rates for strong stimuli. Thus, when we analyzed the amount of multimodal enhancement (as in Fig. 8D) for all these conditions (Fig. 9E) we saw, that for the default and shorter pNeurite lengths (<= 60 µm) inverse effectiveness was most pronounced: weak stimuli showed strong superadditive enhancement (Fig. 9E, red colors), while stronger input powers produced subadditive output (Fig. 9E, blue colors). For increasingly longer pNeurite lengths, the amount of inverse effectiveness was reduced. This means that stronger stimuli still showed superadditive enhancement for longer pNeurites compared with shorter pNeurites. Overall, contours rose diagonally from left to right in Figure 9E indicating that to maintain a certain amount of multimodal enhancement (in number of AP per response) with increasing input powers, increasing lengths of pNeurite were required.

Reducing the decay time constant of apical inputs, which acts as a first-order approximation for the amount of NMDA-type glutamate receptors contributing to the excitatory response, on the other hand had distinct effects on multimodal enhancement in SCN. Obviously, unimodal apical inputs (Fig. 9F) became increasingly less effective with reduced decay time constant, until

apical inputs did not cause any output AP for the chosen range of input rates at all. Here, for a given apical tau-decay (above values of ~45 ms) increasing the apical unimodal input power caused an increase in output rates. The maximal output rate and the slope of the dynamic range depended on the apical tau-decay. Efficacy of basal inputs on the other hand was of course unaffected (Fig. 9G). Similarly, with decreasing apical decay time constant multimodal (Fig. 9H) maximal response rates and, to a lesser extent, the dynamic range was reduced. However, the maximal sum of unimodal responses (Fig. 9I) and the dynamic range of the sum of unimodal responses depended strongly and differently on apical decay-tau. We analyzed the amount of multimodal enhancement (again, as in Fig. 9E) as the difference between unimodal and the sum of unimodal for all these conditions (Fig. 9J). In this analysis, we saw that the amount of inverse effectiveness was correlated with the decay time constant of the apical inputs. This means that for long apical decay time constants the difference in enhancement between weak and strong stimuli was most pronounced. Alternatively, to allow superadditive multimodal enhancement also for stronger stimuli (at the given range of input rates we chose), apical decay time constants needed to be shorter. Overall contours fell diagonally from left to right in Figure 9J, indicating that to maintain a certain amount of enhancement (in AP) with increasing input power decreasing apical decay time constants were required. In reverse, long time constants facilitate the integration of small stimuli. Taken together both the length of the primary neurite (Fig. 9A–E) and the difference in synaptic kinetics between apical and basal (Fig. 9F–J) in the model quantitatively and qualitatively influenced multimodal enhancement in a systematic manner.

Discussion

In this study, we provide novel insight into the role of neuronal morphology and dendrite-specific synaptic properties in multimodal integration. We studied multimodal integration in SCNs. SCNs are part of a complex bottom-up attention network for stimulus selection (Wang et al., 2006; Mysore et al., 2011; Garrido-Charad et al., 2018). They have spatially separated dendrites in retinorecipient layers and in deep layers, where auditory afferents terminate, and transmit visual and auditory information to the isthmic nuclei (Maczko et al., 2006). These nuclei mediate stimulus selection by point-to-point excitatory and wide field inhibitory feedback (Asadollahi et al., 2010; Marín et al., 2012; Garrido-Charad et al., 2018).

In our *in vitro* experiments, we used chicken hatchlings. Chickens are precocial animals with functional auditory and visual systems at the time of hatching. The development of the tectum and the SCNs are finished before hatch (LaVail and Cowan, 1971; Domesick and Morest, 1977; Lever et al., 2014). Thus, in contrast to most other studies on multisensory integration, which used altricial animals like cats (Stein et al., 2014), we do not expect large effects of maturation in SCNs.

SCNs responded to unimodal stimulation of either dendritic area with subthreshold events or APs. In case of bimodal activation, the response enhancement compared with unimodal activation was inversely dependent on the strength of unimodal activation. If unimodal stimuli already evoked APs, bimodal stimulation did not increase the response significantly. Rather, the maximal duration and the shortest latency of unimodal responses was combined. In case of subthreshold unimodal activation, bimodal activation elicited APs. Our *in vitro* data resemble responses of tectal neurons to short electric pulses in the
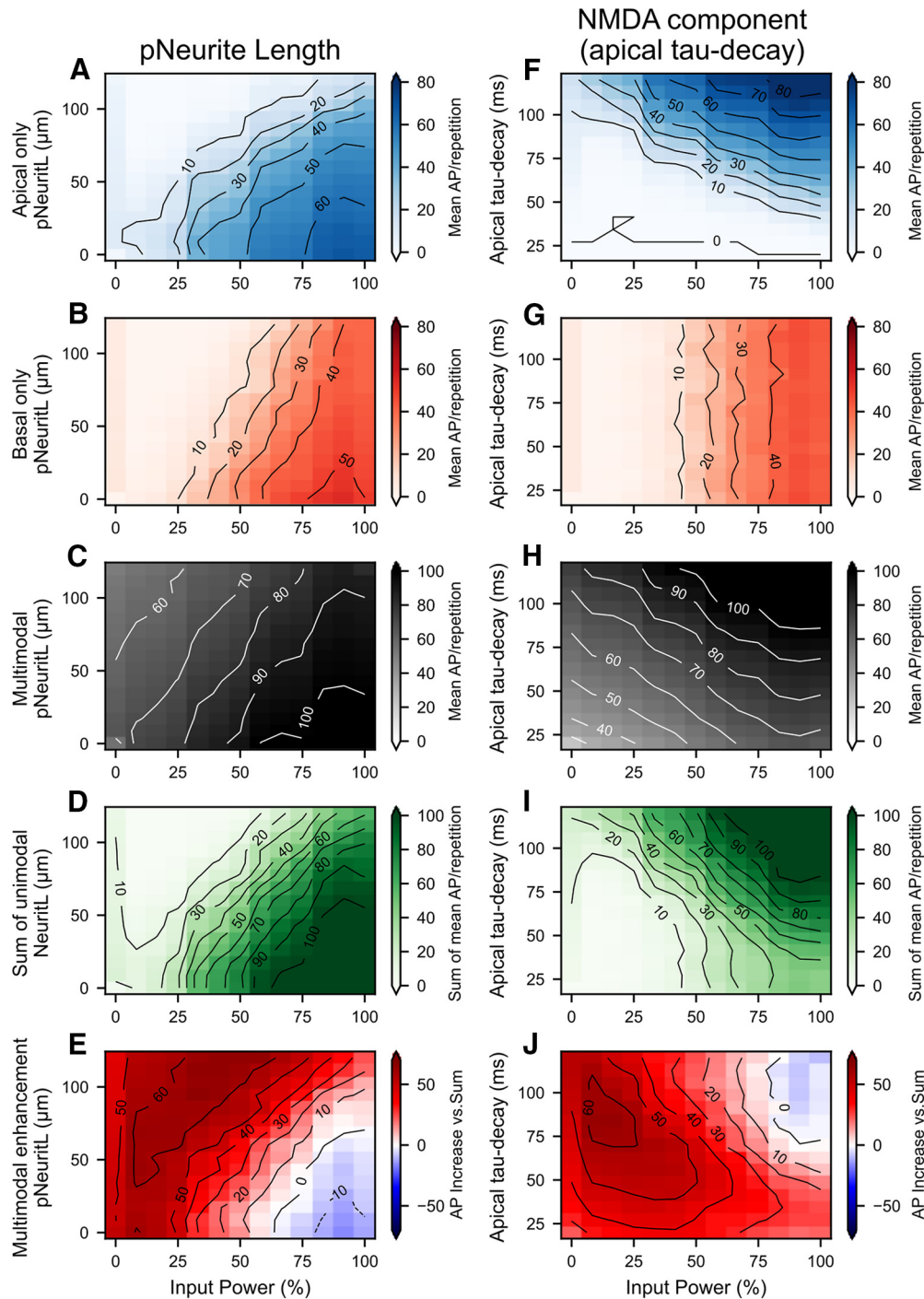
Figure 9. SCN-specific cellular features tune the effectiveness of multimodal enhancement to the input power in the SCN model. Data simulated as in Figure 8 but for varying pNeurite length (*A–E*) and apical decay time constants (*F–J*) shown as 2D plots with input power on the *x*-axis and the varied cellular parameter on the *y*-axis. Color code shows mean number of AP or, for *E*, *J*, AP increase over the sum of unimodal responses. *A*, *F*, Mean number of AP on apical unimodal stimulation per repetition color coded in shades of blue (dark blue = highest AP count) for many stimulus powers (*x*-axis) and pNeurite lengths (*y*-axis, *A*) or apical decay time constants (*y*-axis, *F*). Superimposed interpolated contours (contour function of matplotlib) were derived from the same data as shown in the colormesh in steps of 10 AP/repetition. *B*, *G*, Mean number of AP on basal unimodal stimulation per repetition color coded in shades of red (dark red = highest AP count), presentation as in *A*. *C*, *H*, Mean number of AP on multimodal stimulation per repetition color coded in shades of gray (white = highest AP count). Presentation as in *A*. *D*, *I*, Sum of unimodal responses from *A*, *B* and *F*, *G*, color coded in shades of green (dark green = highest sum), presentation as in *A*. *E*, *J*, Amount of multimodal enhancement as the difference between *C*, *D* and *H*, *I*, color coded in seismic colors (white = no difference, shades of red positive differences, shades of blue negative differences). Presentation otherwise as in *A*.

tadpole. There, only a combination of subthreshold unimodal stimuli but not suprathreshold activation led to multisensory enhancement (Truszkowski et al., 2017). This phenomenon is often called inverse effectiveness (Rowland et al., 2007a; Stein et al., 2009).

In vitro, we were limited to short electric stimuli with only few graduations emulating sensory activity. As these stimuli might result in responses close to threshold or maximum, we have to be careful to draw this conclusion only based on *in vitro* data (Holmes, 2007, 2009).

We developed a realistic multicompartment model to predict multisensory enhancement in SCN in natural stimulus conditions. Most studies on multisensory integration presented sensory stimuli of different strength and duration and compared spike counts (Meredith and Stein, 1986; Stein and Stanford, 2008; Zahar et al., 2009; Stein et al., 2014). We first simulated our *in vitro* experiments and found that bimodal activation decreased the amount of input needed for AP generation. In addition, we tested our model with ongoing, probabilistic stimuli resembling the natural activation pattern of sensory organs. There, we found bimodal superadditive enhancement with reduced first spike latencies resembling *in vivo* data (Rowland et al., 2007b). The amount of enhancement depended inversely on the stimulus strength. Together with the *in vitro* data, it is very likely that SCNs integrate different sensory information leading to multimodal enhancement and shorter response latencies compared with strong visual stimuli *in vivo* following the rule of inverse effectiveness.

The recruitment of NMDARs is involved in the nonlinear integration leading to multimodal enhancement (Binns and Salt, 1996; Rowland et al., 2007a; Cuppini et al., 2010; Truszkowski et al., 2017). To examine the mechanism of integration, we analyzed evoked postsynaptic currents. We found a prolonged response when the apical dendrite was stimulated, and shorter latencies in basal responses. Differences in response kinetics were caused by a dendrite-specific NMDAR contribution specific for the apical postsynaptic response. While others have proposed and shown the importance of NMDARs in the integration process, only Truszkowski et al. (2017) examined how NMDAR affect single cell responses and demonstrated that NMDAR is necessary for the inverse effectiveness in multimodal integration. However, no modality-specific differences in NMDAR contribution were described in that study. Binns and Salt (1996) hypothesized that NMDAR recruitment in neurons of the superior colliculus might be modality specific. Our *in vitro* data demonstrate for the first time a dendrite-specific and thus modality-specific NMDAR content. To analyze the impact of NMDAR on multimodal enhancement, we varied the synaptic kinetics representing the contribution of NMDAR in our model. First, NMDAR decreased the amount of input conductance necessary for AP generation compared with coincidence only. Variation of the NMDAR contribution to the apical response reduced the evoked apical AP rate and reduces the differences in response rate between stimulus intensities. To bimodal stimulation, a higher NMDAR contribution changed the input-output nonlinearity toward a higher sensitivity for weak sensory inputs, which is in line with the findings in tadpoles (Truszkowski et al., 2017). We approximated the NMDA contribution by changing the decay time constant. This disregards voltage-dependent properties of NMDA channels, which would increase the efficacy of apical synapses even further at higher stimulation rates proportional to NMDA content. Thus, our simulation in fact underestimates the apical versus basal differences for higher stimulation rates.

SCNs have an axon initiation segment (AIS) located ∼80 μm away from the soma at the apical dendrite (Ramón y Cajal, 1909; Lischka et al., 2018). Our imaging data support the hypothesis of AP generation at the axon origin. The model reproduced this: in every case, the AP initiation site was located in the primary neurite compartment. However, the exact site of AP initiation depended on the apical to basal ratio and was pulled toward the dominant dendrite. Thus, the model probably produced some minor differences in the spatial dynamics of AP initiation that

may not be entirely realistic. Nevertheless, axon-carrying dendrites (AcDs) usually result in a preferential treatment of the synaptic input arriving at the AcD (Häusser et al., 1995; Thome et al., 2014; Triarhou, 2014; Kole and Brette, 2018). In our model, we see such a preference for apical activation in the lower required input conductance for apical over basal activation and the lower AP threshold for apical stimulation. In the simulated *in vivo* experiments, we counterbalanced this effect for comparability by a reduced average input rate to the apical dendrite. This indicates that visual inputs can be much sparser and are more efficient than auditory inputs. Thus, the physiological and morphologic properties of SCN ensure that visual inputs can always dominate their output.

To date, no study considered the morphology of the integrating neuron. SCNs with their peculiar morphology are ideal to analyze the effect of morphology on multimodal enhancement. We found a negative correlation between the primary neurite length (soma to AIS distance) and evoked AP rate to unimodal and bimodal stimuli indicating a synergistic effect of sodium channels in the AIS and the soma (Lischka et al., 2018) at shorter distances. Comparing nonlinear enhancement at different primary neurite lengths, the range of inverted effectiveness is shifted from a relative low range in short primary neurites to a broad range in long primary neurites even loosing saturation at high input power. Inverted effectiveness seems to be optimal at ∼60- to 80-μm primary neurite length, which is in the range of the AIS to soma distance found in SCN (Lischka et al., 2018). In addition, spatial separation, as opposed to connecting all inputs to one dendrite, further improved multimodal integration in the model. Thus, SCN seemed to be optimized for multimodal integration with a high dynamic range of inverse effectiveness by its morphology and dendrite-specific NMDAR contribution.

Sensory signals of an object have different physical traveling speeds, and neuronal computation speeds differ along the processing pathways but have to be integrated within a temporal window to be perceived as signals from one source (Spence and Squire, 2003; King, 2005). While this is difficult to study in a slice preparation, we varied stimulus presentation in the model. Since differences in visual traveling time are neglectable, we varied basal onset. To include differences in neuronal processing speed, we imposed a modality-specific delay with the visual activation (50 ms pathway delay) lagging auditory activation (20 ms pathway delay) by 30 ms. Here, our model is showing multimodal enhancement over a long time range with maximal enhancement at 68 ms. Presenting this as distance to source, our model is sensitive to bimodal stimuli over a distance of at least 100 m. However, least temporal variance and reduced onset latencies are only given to an approximate distance of 35 m.

Summarizing our findings, we have shown *in vitro* and *in silico* that SCNs are candidates for the integration of different sensory modalities in the tectum. In vitro, we have seen an enhancement predominantly in case of subthreshold stimuli. We further found a dendrite-specific NMDA-component in the apical dendrite. In the model, the NMDA component as well as the particular morphology of SCN provide a broad dynamic range for nonlinear multimodal enhancement with inverse effectiveness. SCN provide also a temporal window for integration over a wide range. Such multisensory integration in SCNs, which are part of a circuit for bottom-up attention, might facilitate the task of detecting the most salient object.

References

Angelaki DE, Gu Y, DeAngelis GC (2009) Multisensory integration: psychophysics, neurophysiology, and computation. Curr Opin Neurobiol 19:452–458.

Asadollahi A, Mysore SP, Knudsen EI (2010) Stimulus-driven competition in a cholinergic midbrain nucleus. Nat Neurosci 13:889–895.

Binns KE, Salt TE (1996) Importance of NMDA receptors for multimodal integration in the deep layers of the cat superior colliculus. J Neurophysiol 75:920–930.

Bradley J, Luo R, Otis TS, DiGregorio DA (2009) Submillisecond optical reporting of membrane potential in situ using a neuronal tracer dye. J Neurosci 29:9197–9209.

Chanda B, Blunck R, Faria LC, Schweizer FE, Mody I, Bezanilla F (2005) A hybrid approach to measuring electrical activity in genetically specified neurons. Nat Neurosci 8:1619–1626.

Cuppini C, Ursino M, Magosso E, Rowland BA, Stein BE (2010) An emergent model of multisensory integration in superior colliculus neurons. Front Integr Neurosci 4:6.

DeBello WM, Knudsen EI (2004) Multiple sites of adaptive plasticity in the owl's auditory localization pathway. J Neurosci 24:6853–6861.

Domesick VB, Morest DK (1977) Migration and differentiation of Shepherd's crook cells in the optic tectum of the chick embryo. Neuroscience 2:477–491.

Dye JC, Karten HJ (1996) An in vitro study of retinotectal transmission in the chick: role of glutamate and GABA in evoked field potentials. Vis Neurosci 13:747–758.

Felch DL, Khakhalin AS, Aizenman CD (2016) Multisensory integration in the developing tectum is constrained by the balance of excitation and inhibition. Elife 5:e15600.

Friedel P, van Hemmen JL (2008) Inhibition, not excitation, is the key to multimodal sensory integration. Biol Cybern 98:597–618.

Garrido-Charad F, Vega-Zuniga T, Gutiérrez-Ibáñez C, Fernandez P, López-Jury L, González-Cabrera C, Karten HJ, Luksch H, Marín GJ (2018) "Shepherd's crook" neurons drive and synchronize the enhancing and suppressive mechanisms of the midbrain stimulus selection network. Proc Natl Acad Sci USA 115:E7615–E7623.

Gingras G, Rowland BA, Stein BE (2009) The differing impact of multisensory and unisensory integration on behavior. J Neurosci 29:4897–4902.

Grill WM Jr (1999) Modeling the effects of electric fields on nerve fibers: influence of tissue electrical properties. IEEE Trans Biomed Eng 46:918–928.

Gutfreund Y, Zheng WM, Knudsen EI (2002) Gated visual input to the central auditory system. Science 297:1556–1559.

Harwell CC, Fuentealba LC, Gonzalez-Cerrillo A, Parker PRL, Gertz CC, Mazzola E, Garcia MT, Alvarez-Buylla A, Cepko CL, Kriegstein AR (2015) Wide dispersion and diversity of clonally related inhibitory interneurons. Neuron 87:999–1007.

Häusser M, Stuart G, Racca C, Sakmann B (1995) Axonal initiation and active dendritic propagation of action potentials in substantia nigra neurons. Neuron 15:637–647.

Hines ML, Carnevale NT (1997) The NEURON simulation environment. Neural Comput 9:1179–1209.

Hines ML, Carnevale NT (2000) Expanding NEURON's Repertoire of Mechanisms with NMODL. Neural Comput 12:995–1007.

Hines ML, Carnevale NT (2001) NEURON: a tool for neuroscientists. Neuroscientist 7:123–135.

Hines ML, Davison AP, Muller E (2009) NEURON and Python. Front Neuroinform 3:1.

Hochbaum DR, Zhao Y, Farhi SL, Klapoetke N, Werley CA, Kapoor V, Zou P, Kralj JM, Maclaurin D, Smedemark-Margulies N, Saulnier JL, Boulting GL, Straub C, Cho YK, Melkonian M, Wong GKS, Harrison DJ, Murthy VN, Sabatini BL, Boyden ES, et al. (2014) All-optical electrophysiology in mammalian neurons using engineered microbial rhodopsins. Nat Methods 11:825–833.

Holmes NP (2007) The law of inverse effectiveness in neurons and behaviour: multisensory integration versus normal variability. Neuropsychologia 45:3340–3345.

Holmes NP (2009) The principle of inverse effectiveness in multisensory integration: some statistical considerations. Brain Topogr 21:168–176.

Kardamakis AA, Pérez-Fernández J, Grillner S (2016) Spatiotemporal interplay between multisensory excitation and recruited inhibition in the lamprey optic tectum. Elife 5:e16472.

Karten HJ, Cox K, Mpodozis J (1997) Two distinct populations of tectal neurons have unique connections within the retinotectorotundal pathway of the pigeon (*Columba livia*). J Comp Neurol 387:449–465.

King AJ (2005) Multisensory integration: strategies for synchronization. Curr Biol 15:R339–R341.

Knudsen EI (1982) Auditory and visual maps of space in the optic tectum of the owl. J Neurosci 2:1177–1194.

Knudsen EI (2007) Fundamental components of attention. Annu Rev Neurosci 30:57–78.

Knudsen EI, Knudsen PF (1983) Space-mapped auditory projections from the inferior colliculus to the optic tectum in the barn owl (*Tyto alba*). J Comp Neurol 218:187–196.

Knudsen EI, Cohen YE, Masino T (1995) Characterization of a forebrain gaze field in the archistriatum of the barn owl-microstimulation and anatomical connections. J Neurosci 15:5139–5151.

Kole MHP, Brette R (2018) The electrical significance of axon location diversity. Curr Opin Neurobiol 51:52–59.

LaVail JH, Cowan WM (1971) The development of the chick optic tectum. I. Normal morphology and cytoarchitectonic development. Brain Res 28:391–419.

Lever M, Brand-Saberi B, Theiss C (2014) Neurogenesis, gliogenesis and the developing chicken optic tectum: an immunohistochemical and ultrastructural analysis. Brain Struct Funct 219:1009–1024.

Lewald J, Dörrscheidt GJ (1998) Spatial-tuning properties of auditory neurons in the optic tectum of the pigeon. Brain Res 790:339–342.

Lischka K, Ladel S, Luksch H, Weigel S (2018) Expression patterns of ion channels and structural proteins in a multimodal cell type of the avian optic tectum. J Comp Neurol 526:412–424.

Luksch H (2003) Cytoarchitecture of the avian optic tectum: neuronal substrate for cellular computation. Rev Neurosci 14:85–106.

Maczko KA, Knudsen PF, Knudsen EI (2006) Auditory and visual space maps in the cholinergic nucleus isthmi pars parvocellularis of the barn owl. J Neurosci 26:12799–12806.

Marín GJ, Durán E, Morales C, González-Cabrera C, Sentis E, Mpodozis J, Letelier JC (2012) Attentional capture? Synchronized feedback signals from the isthmi boost retinal signals to higher visual areas. J Neurosci 32:1110–1122.

Meredith MA, Stein BE (1986) Visual, auditory, and somatosensory convergence on cells in superior colliculus results in multisensory integration. J Neurophysiol 56:640–662.

Meredith MA, Nemitz JW, Stein BE (1987) Determinants of multisensory integration in superior colliculus neurons. I. Temporal factors. J Neurosci 7:3215–3229.

Miller RL, Stein BE, Rowland BA (2017) Multisensory integration uses a real-time unisensory-multisensory transform. J Neurosci 37:5183–5194.

Mysore SP, Asadollahi A, Knudsen EI (2011) Signaling of the strongest stimulus in the owl optic tectum. J Neurosci 31:5186–5196.

Niederleitner B, Luksch H (2012) Neuronal morphology in subdivisions of the inferior colliculus of chicken (*Gallus gallus*). J Chem Neuroanat 44:24–33.

Niederleitner B, Gutierrez-Ibanez C, Krabichler Q, Weigel S, Luksch H (2017) A novel relay nucleus between the inferior colliculus and the optic tectum in the chicken (*Gallus gallus*). J Comp Neurol 525:513–534.

Pena JL, Gutfreund Y (2014) New perspectives on the owl's map of auditory space. Curr Opin Neurobiol 24:55–62.

Pires RS, Britto LR (1997) Distribution of AMPA-type glutamate receptor subunits in the chick visual system. Braz J Med Biol Res 30:73–77.

Ramón y Cajal S (1909) Histologie du système nerveux de l'homme et des vertébrés. Paris:A. Maloine.

Rowland BA, Stanford TR, Stein BE (2007a) A model of the neural mechanisms underlying multisensory integration in the superior colliculus. Perception 36:1431–1443.

Rowland BA, Quessy S, Stanford TR, Stein BE (2007b) Multisensory integration shortens physiological response latencies. J Neurosci 27:5879–5884.

Schmidt A, Bischof HJ (2001) Neurons with complex receptive fields in the stratum griseum centrale of the zebra finch (*Taeniopygia guttata castanotis* Gould) optic tectum. J Comp Physiol A Neuroethol Sens Neural Behav Physiol 187:913–924.

Spence C, Squire S (2003) Multisensory integration: maintaining the perception of synchrony. Curr Biol 13:R519–R521.

Spitzer MW, Bala ADS, Takahashi TT (2004) A neuronal correlate of the precedence effect is associated with spatial selectivity in the barn owl's auditory midbrain. J Neurophysiol 92:2051–2070.

Sridharan D, Knudsen EI (2015) Gamma oscillations in the midbrain spatial attention network: linking circuits to function. Curr Opin Neurobiol 31:189–198.

Stein BE, Stanford TR (2008) Multisensory integration: current issues from the perspective of the single neuron. Nat Rev Neurosci 9:255–266.

Stein BE, Stanford TR, Ramachandran R, Perrault TJ, Rowland BA (2009) Challenges in quantifying multisensory integration: alternative criteria, models, and inverse effectiveness. Exp Brain Res 198:113–126.

Stein BE, Stanford TR, Rowland BA (2014) Development of multisensory integration from the perspective of the individual neuron. Nat Rev Neurosci 15:520–535.

Stein BE, Stanford TR, Rowland BA (2020) Multisensory integration and the Society for Neuroscience: then and now. J Neurosci 40:3–11.

Thome C, Kelly T, Yanez A, Schultz C, Engelhardt M, Cambridge SB, Both M, Draguhn A, Beck H, Egorov AV (2014) Axon-carrying dendrites convey privileged synaptic input in hippocampal neurons. Neuron 83:1418–1430.

Triarhou LC (2014) Axons emanating from dendrites: phylogenetic repercussions with Cajalian hues. Front Neuroanat 8:133.

Truszkowski TL, Carrillo OA, Bleier J, Ramirez-Vizcarrondo CM, Felch DL, McQuillan M, Truszkowski CP, Khakhalin AS, Aizenman CD (2017) A cellular mechanism for inverse effectiveness in multisensory integration. Elife 6:e25392.

Verhaal J, Luksch H (2016a) Neuronal responses to motion and apparent motion in the optic tectum of chickens. Brain Res 1635:190–200.

Verhaal J, Luksch H (2016b) Multimodal integration in the chicken. J Exp Biol 219:90–95.

Wang Y, Luksch H, Brecha NC, Karten HJ (2006) Columnar projections from the cholinergic nucleus isthmi to the optic tectum in chicks (*Gallus gallus*): a possible substrate for synchronizing tectal channels. J Comp Neurol 494:7–35.

Weigel S, Luksch H (2012) Spatiotemporal analysis of electrically evoked activity in the chicken optic tectum: a VSDI study. J Neurophysiol 107:640–648.

Weigel S, Flisikowska T, Schnieke A, Luksch H (2014) Hybrid voltage sensor imaging of eGFP-F expressing neurons in chicken midbrain slices. J Neurosci Methods 233:28–33.

Woodson W, Reiner A, Anderson K, Karten HJ (1991) Distribution, laminar location, and morphology of tectal neurons projecting to the isthmo-optic nucleus and the nucleus isthmi, pars parvocellularis in the pigeon (*Columba livia*) and chick (*Gallus domesticus*): a retrograde labelling study. J Comp Neurol 305:470–488.

Wylie DR, Gutierrez-Ibanez C, Pakan JM, Iwaniuk AN (2009) The optic tectum of birds: mapping our way to understanding visual processing. Can J Exp Psychol 63:328–338.

Yamagata M, Weiner JA, Dulac C, Roth KA, Sanes JR (2006) Labeled lines in the retinotectal system: markers for retinorecipient sublaminae and the retinal ganglion cell subsets that innervate them. Mol Cell Neurosci 33:296–310.

Zahar Y, Reches A, Gutfreund Y (2009) Multisensory enhancement in the optic tectum of the barn owl: spike count and spike timing. J Neurophysiol 101:2380–2394.